REPORT DOCUMENTATION PAGE

AFRL-SR-AR-TR-02-

0047

Public reporting burden for this collection of information is estimated to average 1 hour per response, including the time for reviewing instructions, data needed, and completing and reviewing this collection of information. Send comments regarding this burden estimate or any other as; this burden to Department of Defense, Washington Headquarters Services, Directorate for Information Operations and Reports (0704-018, 4302. Respondents should be aware that notwithstanding any other provision of law, no person shall be subject to any penalty for failing to valid OMB control number. PLEASE DO NOT RETURN YOUR FORM TO THE ABOVE ADDRESS.

1. REPORT DATE (DD-MM-YYYY) 07/16/2002	2. REPORT TYPE Final Technical Report	3. DATES COVERED (From - To) 10/01/1999-09/30/2001

4. TITLE AND SUBTITLE The Control of Separation from Curved Surfaces and Blunt Trailing Edges	5a. CONTRACT NUMBER
	5b. GRANT NUMBER F49620-00-1-0070
	5c. PROGRAM ELEMENT NUMBER

6. AUTHOR(S) Israel J. Wygnanski, Professor	5d. PROJECT NUMBER
	5e. TASK NUMBER
	5f. WORK UNIT NUMBER

7. PERFORMING ORGANIZATION NAME(S) AND ADDRESS(ES) The Department of Aerospace Tucson, AZ 85721 and Mechanical Engineering The College of Engineering and Mines The University of Arizona	8. PERFORMING ORGANIZATION REPORT NUMBER

9. SPONSORING / MONITORING AGENCY NAME(S) AND ADDRESS(ES) AFOSR/NA 801 N. Randolph St, Room 732 Arlington, VA 22203-1977	10. SPONSOR/MONITOR'S ACRONYM(S)
	11. SPONSOR/MONITOR'S REPORT NUMBER(S)

12. DISTRIBUTION / AVAILABILITY STATEMENT
Approved for Public Release - Distribution is Unlimited

20020816 044

13. SUPPLEMENTARY NOTES

14. ABSTRACT

The project that was initiated in the fall of 1999 encompasses three exploratory studies:
(1) A pulsed wall jet over a curved surface in the absence of an external stream
(2) Pulsation emanating from a circular cylinder in streaming flow.
(3) The application of active flow control to an airfoil having a divergent trailing edge

The report will cover all three experiments although most progress (beyond the exploratory stage) was made on understanding the wall jet flowing over a convex surface. Some of the experimental work on this project was initiated prior to the last funding period but data analysis took more time some of the results have been discussed in interim progress reports. The other investigations are still ongoing at a lower pace.

15. SUBJECT TERMS

16. SECURITY CLASSIFICATION OF:			17. LIMITATION OF ABSTRACT	18. NUMBER OF PAGES	19a. NAME OF RESPONSIBLE PERSON Israel J. Wygnanski
a. REPORT UNCLASSIFED	b. ABSTRACT UNCLASSIFIED	c. THIS PAGE UNCLASSIFIED	UNCLASSIFIED	47	19b. TELEPHONE NUMBER (include area code)(520)621-6089

Standard Form 298 (Rev. 8-98)
Prescribed by ANSI Std. Z39.18

THE CONTROL OF SEPARATION FROM CURVED SURFACES AND BLUNT TRAILING EDGES.

AFOSR GRANT F 49620-00-1-0070

Final Technical Report Covering Period 10/01/1999-09/30/2001

Israel J. Wygnanski
AME Department
The University of Arizona, Tucson

Overview

The project that was initiated in the fall of 1999 encompasses three exploratory studies:
  (1) A pulsed wall jet over a curved surface in the absence of an external stream
  (2) Pulsation emanating from a circular cylinder in streaming flow.
  (3) The application of active flow control to an airfoil having a divergent trailing edge

The report will cover all three experiments although most progress (beyond the exploratory stage) was made on understanding the wall jet flowing over a convex surface. Some of the experimental work on this project was initiated prior to the last funding period but data analysis took more time some of the results have been discussed in interim progress reports. The other investigations are still ongoing at a lower pace.

ON LARGE STREAMWISE STRUCTURES IN A WALL JET THAT FLOWS OVER A CIRCULAR CYLINDER.

ABSTRACT

This paper describes a search for large streamwise vortices in a turbulent wall jet flowing over a convex surface. The existence of these vortices was suspected but not observed because they meander in time. A particle image velocimeter enabled the mapping of these vortices establishing their circulation and its evolution in the direction of streaming. Also the turbulent characteristics surrounding a pair of counter-rotating vortices were observed in a frame of reference that is statistically stationary relative to the vortex core. Although no attempt was made to compare the experimental findings with a stability model, due to possible concomitant interactions of various instabilities in this flow, it is anticipated that the differences in the evolution of the mean flow are due to a centrifugal instability.

1. Introduction

The effects of streamline curvature on turbulence generated in mixing layers were investigated by Margolis & Lumley [1965] and by Wyngaard et al. [1968]. Bradshaw [1969] and more recently Patel & Sotiropoulos [1996] reviewed the available literature that is concerned with the effects of streamline curvature in wall-bounded and free, turbulent shear flows. In his opening statement Bradshaw wrote:
"Streamline curvature ... produces surprisingly large changes in the turbulent structure of shear layers. These changes are usually an order of magnitude more important than ... explicit terms appearing in the mean motion equations for curved flows."

Observations made by Neuendorf & Wygnanski [1999, thereafter referred to as N&W] in a turbulent wall jet that flows over a circular cylinder are in total agreement with Bradshaw's statement. N&W showed that:

(i) The surface pressure on the cylinder is approximately constant over one third of its circumference (i.e. from the nozzle where $\theta=0°$ to $\theta=120°$, thereafter the pressure increases until it attains the ambient pressure where the flow separates around $\theta=220°$, see N&W).

(ii) The normalized mean velocity profile is almost identical in the constant pressure region to its counterpart on a flat surface but the rate of spread of the flow over the cylinder is much larger.

(iii) The turbulent intensities are <u>not</u> in equilibrium with the mean motion, in contrast to the plane
wall jet where they clearly are in such equilibrium. They amplify under the influence of curvature, with the streamwise and radial normalized components
$(\sqrt{u'^2}/U_{max}, \sqrt{v'^2}/U_{max})$ increasing their value within the constant pressure region by more than 50% over and above the plane flow. The comparison was made at corresponding locations determined by the mean velocity in the jet (i.e. at

identical y/y_2, where y_2 represents the width of the jet) The spanwise component, ($\sqrt{\overline{w'^2}}/U_{max}$) on the other hand, is not directly affected by curvature and increases near the surface due to second order effects.

(iv) The mean velocity profiles, measured close to the separation location, do not containthe classical tale tell signs of impending separation (i.e. new inflexion points) as they always do in two-dimensional boundary layers. Since in the present experiment the mean flow is two-dimensional, one may speculate that the separation may be occurring in cells that are not stationary along the span.

Examination of the Reynolds averaged transport equations describing the production of each of the three components of the turbulent intensity and of the Reynolds stress do not provide an adequate explanation of the observations made. On the other hand, the presence of quasi-stationary streamwise vortices could generate three-dimensional distortions in the mean flow that could give rise to the large differences observed between the plane and the curved wall jets. The existence of streamwise vortices resulting from centrifugal instability is anticipated in turbulent, curved shear flows (Tani 1962, Patel et al. 1996) but they were not observed in an unambiguous manner. Tani in his seminal investigation of a boundary layer over a concave surface in the absence of pressure gradient, observed the existence of longitudinal vortices in laminar flow, but he could only guess their presence and estimate their scale in turbulent flow. One might have also suggest that these vortices, whose presence was only inferred from a velocity signal, were generated by upstream protuberances. To date, streamwise vortices were not observed in a wall jet flowing over a convex surface, in spite of the meticulous search by Guitton [1970] for the tale telling spanwise variations in the surface shear stress. Both Guitton (1970) and Fekete (1963) observed the great sensitivity of the flow to imperfections at the nozzle-lip that resulted in steady spanwise variations in the mean motion implying a predisposition of the flow to streamwise vortices. Such a predisposition may exist in a boundary layer as well, resulting in streamwise vortices triggered by roughness spots or by vortex generators.

Two point correlation measurements accompanied by flow visualization on the curved wall-jet (Likhachev, Neuendorf, and Wygnanski, 2001), suggested the presence of streamwise vortices in the flow but these observations lacked the quantitative measures needed to define the character and strength of these vortices. Multi-point correlation techniques in general, that evolved around the hot-wire anemometer, enable one to construct a simple model of a time averaged eddy consistent with the measurements, but they provide no proof for the existence of such an eddy at any moment in the flow (see Townsend 1956 & 1973). For this reason an investigation using a particle image velocimeter (hereafter referred to as PIV) was initiated, as it provides instantaneous information about the state of the flow in a plane that is illuminated by a laser-light-sheet and may enable one to map the flow in and around an entire vortex.

Coherent structures in turbulent shear flows are assumed to be a product of the leading instabilities. They therefore, dominate the turbulent transport of momentum and heat across the flow and alter its mean character. Some of the instabilities are time dependent (e.g. Tollmien Schlichting instability) while others generate stationary spatial undulations

(e.g. Gortler instability) that lead to the distortion of the basic state (Saric 1994). Most second order instabilities contain perturbations of both categories. Since the curved wall jet is susceptible to numerous instabilities that may develop concomitantly, the weakly non-linear approach that relies on an establishment of a hierarchy of modes may not be applicable. The difficulties are compounded by the fact that the linear approach is not applicable to the centrifugal instability in this slightly divergent, open flow system. In fact a dominant mode may only be achievable through external intervention that enhances a specific instability above the rest. For this reason a search for a model accentuating a specific instability mechanism is premature and may be detrimental to the broad understanding of the flow. In order to describe time dependent, coherent structures in turbulent flow statistically, one has to ensemble-average the data collected in a meaningful way. This was achieved by introducing small amplitude periodic perturbations into the basic state at a priori known, or assumed to be known dominant mode. The seeds for technique were sewn by Schubauer and Skramstad (1948) who introduced periodic perturbations in a laminar boundary layer to trigger a theoretically known instability, i.e. to initiate T.-S. waves. This breakthrough technique became a major diagnostic tool for studying flow-stability and it was extended to free turbulent shear flows, like the mixing layer (Oster et al., 1978; Gaster et al., 1985). By using the external excitation as a diagnostic tool one may minimize some major problems stemming from imperfect periodicity, phase jitter, and variation in size and in shape of the individual structures. Furthermore, it provides a phase reference enabling the subsequent triple decomposition of the data into time-mean, coherent and random constituents. However, since most externally introduced perturbations, enhance the amplitude of some pre-selected instabilities above and beyond the level that they would have achieved naturally, they also modify the basic state. This is an asset when a modification of the mean flow is required, but it is a detriment when one attempts to understand a flow whose basic state and its leading instability are affected concurrently. The wall jet flowing over a convex surface is a case in point (Saric, 1994). Thus the imposition of fixed vortices on the flow through vortex generators or jets (e.g. Matsson 1995) may be artificial and a less intrusive method is required. Pattern recognition schemes in conjunction with a PIV provide a tool that is capable of educing large eddies stemming from an instability while being totally non-intrusive.

2. Brief Description of the Experimental Apparatus

The experiments were performed in a facility built at McGill University by Professors Newman and Fekete. Although it is described in N&W, a cross sectional view of the facility is shown in figure 1. It was evident from the beginning that flow quality depends significantly on the design of the facility. Many experimental setups favored an external settling chamber and nozzle that interfered with the wall jet after the latter turned 180° around the surface of the cylinder. As a consequence, the flow developed early three-dimensionalities that resulted in a shorter constant pressure region and earlier flow separation.

The cylinder was mounted in a steel framework, about 1.30 m above the floor, inside two large end-plates that allowed it to be rotated about its axis in order to vary the

4

downstream location of the measurements. The large clearance between the cylinder and the floor or the ceiling helped to establish a steady outer boundary condition of $U_\infty = 0$ regardless of the rotational angle of the cylinder. The independence of the flow field from the angle of rotation was established by repeated surface pressure measurements and hot-wire measurements at constant distance from the nozzle, θ, but at various angles of nozzle relative to fixed laboratory coordinates. No effect on either pressure or velocity was observed. The two-dimensionality of the mean flow throughout the self-similarity region ($\theta = 40° - 120°$) was checked and validated by a momentum balance (see N&W).

The concept of PIV is fairly simple. The fluid is seeded with small tracer particles and illuminated twice by a thin sheet of monochromatic light. The light scattered by the tracer particles is recorded on a CCD, cross-correlation camera. The information stored can be extracted at a later time.

The optical set-up used for this investigation consisted of two Nd:Yag lasers, a light-guide system and light-sheet optics. Each pulse has a duration of 6-7ns, and a total energy of 650mJ. The pulse energy stability is good with a variance that is smaller than 3%. By mounting all optical components onto a single rigid base-plate a long term beam overlap and pointing stability is ensured. The optimum pulse repetition rate is 3 Hz only and therefore the temporal resolution of important flow events is impossible. The delay between the two laser pulses is controlled by electronic delay circuitry and verified by measuring the Q-switch synchronization of the laser power supplies. The recording system consists of a KODAK CCD Camera, that has a spatial resolution of over one million pixels. Each pixel measures nine microns square with a 60 percent fill factor using a microlens. Image enhancement circuitry assures maximum image uniformity. In contrast to the more common interline transfer CCD sensor this sensor is capable of shuttering and storing the entire array of pixels, not just every other line. Thus, this sensor offers full vertical resolution when the CCD is used in shuttered mode. Two different lenses of 105mm and 50mm focal length were used. The distortion and magnification of the system was measured by recording test images of known size and shape. Within the accuracy of the system the results showed no errors.

Oil droplets, generated by a commercially available atomizer were used as tracer particles. The atomizer incorporates built-in dilution air, useful in establishing an output particle concentration range. Several liquids were tested and the best results were achieved with a solution of one part polyethylene-glycol (PEG600) dissolved in 5 parts water. The average particle diameter was approximately 1μm. The mean diameter depends largely on the type of liquid being atomized. There is little sensitivity to the operational pressure of the atomizer. The advantage of PEG is that it remains suspended in air at rest for a very long time (>1hour) and it is non-toxic. The goal of good flow seeding is to obtain uniform seeding density in the region of interest and consequently the entire room was filled with smoke prior to the acquisition of data.

To produce a high resolution displacement field from the digital image pairs an image-matching approach described by Lourenco & Krothapalli et al. (1998) was employed. This algorithm enabled us not only to resolve accurately large gradients in the velocity

field but also permitted measurements close to the surface. For further information refer to Krothapalli *et al.* (1999).

3. Pattern Recognition Technique

The first step in recognizing a pattern requires enhancement of the acquired image. This is the most subjective part of the pattern recognition process and it necessitates a cautious design of the enhancement operator. The effectiveness of enhancement process depends on the extent and accuracy of the prior knowledge that defines the nature of the data and the reasons for its degradation. The spectral characteristics of a signal are especially important for designing a filter and these characteristics can be easily obtained by the application of a Fourier transform to the signal acquired. In order to separate the waveform of the coherent structure from the noise, a narrow band-pass filter must be applied at the given peak frequency. The same procedure is followed now to the two-dimensional, PIV vorticity picture. The two-dimensional Fourier transform and its inverse transform are defined below:

$$F(\zeta_2, \zeta_3) = \int_{-\infty}^{\infty} \int_{-\infty}^{\infty} f(y,z) \exp[-j2\pi(y\zeta_2 + z\zeta_3)] dy dz$$

$$f(y,z) = \int_{-\infty}^{\infty} \int_{-\infty}^{\infty} F(\zeta_2, \zeta_3) \exp[-j2\pi(y\zeta_2 + z\zeta_3)] d\zeta_2 d\zeta_3$$

(1) & (2)

where F represents a two-dimensional Fourier Transform & f represents its inverse.

Since the units of ζ_2 and ζ_3 are also reciprocals of y and z, just as the frequency ω is reciprocal of the time t, ζ_2 and ζ_3 may also be referred to as frequencies that describe changes per unit length. The independent variables y, z, ζ_2 and ζ_3 in the equation above are chosen to be consistent with the coordinate system of the PIV data. Furthermore, the spatial frequency ζ_3 is proportional to $1/\lambda_z$, where λ_z is the spanwise wavelength of the most probable streamwise structure. Figures 2 & 3 show an instantaneous vorticity contour image f(y,z) and its Fourier transform $F(\zeta_2, \zeta_3)$, respectively. The Fourier transform $F(\zeta_2, \zeta_3)$ is plotted in wrap-around order with the origin - mean vorticity of the whole image - in the center of the plot. It can be seen in figure 3 that the vorticity has most of its energy concentrated in a small region in the frequency domain near the origin and along the ζ_2 and ζ_3 axis. One reason for the energy concentration near the origin is that the velocity field contains large regions where the vorticity changes slowly (the fluid is viscous). This is might be related to the weak nature of the observed longitudinal structures, that do not create significant gradients in the flow. The vorticity concentration along the ζ_2 and ζ_3 axis is a direct outcome of the rectangular window used to obtain a finite-extent of the image. The energies associated with these artifacts are small and they do not affect the more important low frequency regions in the image (figure 3). Therefore, it will not be necessary to apply a window function to the data prior to the transformation.

6

A more quantitative presentation of the Fourier transform $F(\zeta_2,\zeta_3)$ is given in figure 4 that represents a cut through the origin in the positive ζ_2-direction. This information is most helpful for the design of a proper filter because it describes the vorticity spectrum as a function of the spanwise frequency $F(\zeta_3)$ at $\zeta_2 = 0$, which represents the spanwise direction z. The dashed line in this figure represents the Fourier transform of the single realization shown in figure 2, the solid line shows the mean curve for the complete data-set containing 500 images. In an analogous fashion to the one-dimensional example presented above, a finite impulse response (FIR) filter is used to reduce the influence of random noise on the image. After the filter was designed, it was applied to the rest of the images. Instead of using a numerically cumbersome convolution of the impulse response of the filter function $h(y,z)$ with the individual images $f(y,z)$, the convolution theorem suggested that the filtering is the convolution of both functions. This method appreciably reduces the computational effort. In the present case a 64×64 array was used and the smoothed vorticity contours are shown. The single example that was originally plotted in figure 2 is re-plotted after being low-pass filtered in figure 5. The difference between these two images is apparent. The vorticity distribution in the unfiltered image exhibits a larger number of strong but small vortices while the low-pass filtered data (see figure 5) shows fewer ones, but it does not alter the character of the image. Overlaid on top of the contours are ellipses, representing the approximate size, shape and location of several vortices, reconstructed from the vector field. Note for example that vortex A exhibits two strong vorticity peaks in the unfiltered image although the velocity field suggests the presence of a large single vortex. Although the filter reduces the peak levels of the vorticity in a single image, the longitudinal structures are not affected and only the signal-to-noise ratio is enhanced. After all the images were low-pass filtered, vorticity levels that were less than 20% of the maximum were equated to zero. This "noise clipping" was performed to provide additional immunity from noise. Similar to the filter design, the level of clipping depends on the extent of our prior knowledge about the noise characteristics of the data. Several tests with threshold values ranging from 5% to 50% of the maximum value were therefore performed. Two criteria that are important for the following *Feature Extraction* were considered. First, the shape of the vortices had to be preserved by the remaining vorticity field and second, that neighboring vortices remained separated as they were before the elimination of data that did not meet the threshold criteria (figure 6). The tests showed that a threshold level of 20% of the maximum value fulfilled those requirements best.

A completely different identification approach was also tested and compared with the eduction procedure outlined above. It is more intuitive and thus, perhaps physically more acceptable. One may start an identification procedure by recognizing that the presence of counter-rotating vortices will change the sign of the w-component of velocity along the span of a single PIV picture (figure 7a,b). The periodicity in the w signal can best be ascertained near the surface where it is fairly regular even without smoothing (figure 7c). This enabled the determination of the spanwise location of the "zero-crossings" for each realization. Statistical ensemble of these crossings with a given slope provided histograms representing the average location of the boundary between adjacent vortices having opposing signs of vorticity (figure 7d-f). These boundaries represent an origin of an ejection or a "fountain-flow" that collects fluid from the surface and ejects it outward

or, an impingement region that brings outer fluid to the surface (figure 7b). Shifting the individual realizations to the average location of such a boundary and then obtaining the average vorticity field shows clearly the existence of the counter-rotating pairs of vortices. This procedure prevents the smearing that occurs in the simple averaging of images that results in the disappearance of streamwise vortices. It provides, however only the first step in a pattern recognition scheme because the educed vortices remain smeared in y-direction (normal to the surface) across the entire ensemble-averaged PIV picture that spans the width of the wall jet. In this scheme, one also faces an arbitrary decision whether to shift _all_ the images toward a single ejection or a single impingement region or group them according to their preferred spanwise locations. There are on the average three pairs of vortices per realization in the cross section chosen and the histograms showing the preferred location of their fountains is shown in figures 7d to 7f. Because of the relatively small sample used in the statistics, the average vorticity contours of each pair of vortices may differ slightly along the span. Thereafter one has to correlate the individual, low-pass filtered realizations with the initially educed pattern, whereupon the y-location of the maximum correlation is determined as well and the histogram of these locations is determined. A new ensemble-average is created, by shifting first all the events in y and in z direction simultaneously to an average representative location where the vortex-pair resides. The ensuing average vorticity contours are shown in figure 7g. Various schemes of image enhancement were tried and to the first order of approximation, they rendered almost identical results. In the future a three-component PIV system may be used broadening the focus of the investigation and in that case a preferred scheme might emerge. The results described below use the double Fourier decomposition technique.

4.   Cross Sectional Mean Flow Distribution

The plane of illumination used the presently is in the cross-flow plane. The jet is thereby orthogonal to the laser sheet. The PIV measurements were conducted at four equally spaced streamwise locations. The first three stations were in the self-similar region at $\theta = 40°$, $80°$, and $120°$, the final station was in the adverse pressure gradient region where the local surface pressure had increased by 25% relative to its constant value upstream, i.e. at $\theta = 160°$. Unfortunately, the present experimental setup did not allow data acquisition at any location further downstream. 500 images were acquired at each measuring position and averaged to ensure convergence of the results. The measurements yielded two component of mean velocity $\bar{v}$, $\bar{w}$, and three components of the Reynolds stress tensor $\sqrt{\overline{v'^2}}/U_{max}$, $\sqrt{\overline{w'^2}}/U_{max}$, and $\overline{v'w'}/U_{max}$. Based on the measurement of the $\bar{v}$ and $\bar{w}$ components of velocity, the streamwise component of the mean vorticity Ω_x was computed using central differences. Most of the PIV results will be presented in contour form; see, for instance, figure 10a. The horizontal axis represents the cylinder surface and the origin at (0,0) coincides with the center of its span. The profile next to the contour plot, when given, represents the spanwise average of the plotted component - in the case of figure 8b it is $\bar{v}/U_{max}$. The velocities are normalized by the local maximum velocity, U_{max}, and the length-scales by the local half-width, y_2.

Before discussing the streamwise development of the flow, the accuracy of the PIV data was assessed by comparison with hot-wire measurements made at the same θ location. Hot wire and PIV data is shown for $\theta = 80°$, where the hot-wire measurements were made along the center span of the cylinder. Single wire data, X-wire or V-wire data were used for this comparison. The two different dual-wire probes were used to minimize the influence of the mean velocity gradient in the wall boundary layer. The mean vorticity, Ω_x, contours and the local mean velocity vectors in the cross-sectional plane ($\theta = 80°$) are plotted in figure 8a. Note that in the outer part of the wall jet ($y/y_2 > 1$) the entrained flow, having $\bar{v} < 0$, is nearly perfectly two-dimensional. Most of the velocity vectors are of equal length across the span, they are parallel and directed toward the wall. The vectors in the boundary layer are oriented in the opposite direction. A $\bar{v}$-component "stagnation line" is formed between those two regions at approximately $y/y_2 = 1$. The term "stagnation line" might be misleading as it applies to the cross-plane flow only, but it is used here to emphasize the region where the secondary velocities, $\bar{v}$ and $\bar{w}$, equal zero. The strong entrainment in the outer shear layer becomes more apparent in figure 8b where the averaged velocity profile $\bar{v}/U_{max}$ is shown. Note that the radial component $\bar{v}$ exceeds 5% of U_{max} even far beyond $y = 2y_2$. The streamwise component $\bar{u}$, measured with a PIV (using illumination in the R, θ plane) almost vanished at this location (figure 9). A significant discrepancy in the results for the radial velocity component generated by the two measurement systems is also shown in figure 9 (for more details about the hot-wire technique used here see N&W). The differences reflect the well-known problems of hot-wire anemometry in highly intense turbulent flows. The large errors in the outer shear layer region stem from the fact that both $\bar{v}/\bar{u}$ and $u'/\bar{u}$ are of order unity. This may even lead to rectification of the hot-wire signal or exceedence of the calibration table. The mean velocities calculated from the continuity equation (black solid triangles in figure 9) are based on single wire probe measurements of the streamwise velocity component assuming that the mean flow is two-dimensional. The PIV results agree quite well with the calculated data up to $y/y_2 = 1.7$, thereafter the two curves diverge due to the shortcomings of the hot wire anemometry. The PIV is a better instrument in this case, as long as the seeding is sufficiently homogeneous and the velocity component normal to the plane of illumination is small.

Contours of the normalized turbulence intensities, $\sqrt{\bar{v'^2}}/U_{max}$ and $\sqrt{\bar{w'^2}}/U_{max}$, are shown in figure 10, contours of $\bar{v'w'}/U_{max}$ were measured but their value was too small to be of significance. The mean secondary shear stress averaged over the span, $\bar{v'w'}/U_{max} = 0$ across the flow. There is an excellent uniformity of the turbulent intensities along the span in the outer region while some non-uniformity emerges in the wall boundary layer. One has to bear in mind, however, that the results represent an average of 500 images only. This number represents an ensemble average that is less than one percent of the typical time series used in creating averages with a hot wire anemometer. The hot-wire measurements taken in the mid span plane are plotted in figures 10b and d for comparison. The agreement between the two methods of measurement is good although differences occur in the outer and inner extremities of the flow. In the outer region the CTA is mostly in error while in the inner region it is probably the PIV. The discrepancy in the wall region

may be attributed to lower spatial resolution of the PIV system and to surface reflections that could not be entirely eliminated. Surface reflections prevented the gathering of useful data near the wall. The hot-wire systems using V-wire probes is useful near the surface. Since the focus of this study pertains to the development of large-scale longitudinal structures, the apparent deficiencies of the PIV system in the vicinity of the wall are inconsequential.

5.   Spatial Triple-Decomposition of PIV Data

The large effects of curvature on the evolution of the wall jet are attributed to the existence of longitudinal structures that also increase the production of $\overline{v'^2}$, $\overline{w'^2}$. The increase of the streamwise component, $\overline{u'^2}$, is considered as being a second order effect, that is also attributed to the longitudinal structures. However, since the ensemble-averaged results from the PIV system did not show "significant" spanwise non-uniformities in mean velocities and in turbulent intensities a suggestion could be made that spatially steady longitudinal structures do not exist in this flow. Two-point-cross-correlation measurements using a "V" type probe and theoretical considerations suggest otherwise (Likhachev, Neuendorf, and Wygnanski, 2001). Apparently, these counter-rotating longitudinal structures are sufficiently unsteady so as not to produce any mean-spanwise variations in the flow, but they are regular enough to generate significant negative two-point correlations.

In order to map the longitudinal structures in this turbulent wall jet and assess their contribution to the flow, the pattern recognition methods that were discussed above were used. Since the PIV provides instantaneous information in the plane of illumination the decomposition of the equations of motion has to take advantage of this fact. The conventional Reynolds-averaging or double-decomposition (DD) of the equations of motion does not discriminate between coherent, large-eddies and incoherent ones. It describes an instantaneous variable ξ in terms of its mean, $\overline{\xi}$, and a fluctuating ξ' components.

$$\xi(x,y,z,t) = \overline{\xi}(x,y,z) + \xi'(x,y,z,t)$$

(3)

In order to extract the coherent constituent of the signal from the stochastic background of a turbulent flow-field one has to sample and compare the recurrent events that have a certain similarity. Pattern extraction from a sequence of sampled data can fulfill this requirement. Zhou *et al.* (1996), for instance, introduced a pattern recognition technique to provide detailed information about the mechanisms involved in a turbulent energy cascade occurring in a plane wall jet. Their technique was tailored to the needs of processing temporal information generated at a single point in space (i.e. acquired by a hot-wire probe). The key to their method is the application of pattern extraction in the time (frequency) domain, where all the significant Fourier components of an individual realization were extracted from a relatively short sample of data instead of the entire duration of the available time series. Unfortunately, this technique is not suited for processing instantaneous information in space and only such information can currently be provided by a PIV in air due to the slow repetition rate of the pulsed laser. Therefore, the

temporal type of triple decomposition, (TTD), had to be replaced by a spatial triple decomposition (STD) assuming that the flow is stationary. Regardless of the differences between the TTD and the STD, the traditional notation will be used for the triple-decomposition of an instantaneous variable ξ, as suggested by Hussain (1983)

$$\xi(x,y,z,t) = \bar{\xi}(x,y,z) + \tilde{\xi}(x,y,z,t) + \xi'(x,y,z,t)$$

(4)

and define the STD as

$$\xi(x,y,z,t) = \bar{\xi}(x,y,z) + \tilde{\xi}(x,y,z) + \xi'(x,y,z,t)$$

(5)

The first term on the right-hand side $\bar{\xi}$ is the stationary component of the variable that ξ, $\langle\xi\rangle \equiv \bar{\xi} + \tilde{\xi}$ that represents the sum of the stationary and the coherent components of ξ is defined differently for TTD and STD. In the former case the flow is usually artificially excited to provide a time reference signal. If the excitation is periodic, $\langle\xi\rangle$ represents the phase locked average. When the excitation is provided by a pulse, then the time delay following its initiation may be used to generate the ensemble average. Otherwise some temporal pattern recognition is required, to be followed by a procedure akin to the VITA (variable interval time average) technique (see Blackwelder & Kaplan 1972). In the STD case a spatial pattern recognition method, that is analogous to the VITA technique has to be used. In both cases ξ' is the remainder and it represents the random (not recognized as coherent) constituent. As a consequence of the different decomposition and pattern recognition criteria, the various coherent and random constituents resolved by TTD and STD will be different. The reason for this is that the flow in TTD notation is viewed as by an observer fixed in space while in the STD notation, the observer moves with the core of a recognized structure (or in this case a streamwise vortex). The vortex core stands still and only its strength and its size varies in space. The advantage of this representation is obvious; it enables one to discriminate between the high frequency small scale turbulence and the slow (low frequency) meander of large longitudinal structures. The latter will appear in the second term on the right-hand side.

The following figures represent but a fraction of the actual measurement window selected for the sake of clarity. They represent an approximate spanwise domain $\Delta z = 2.2 y_2$ around the centerline of the cylinder (e.g. figure 11). The absolute width of the measured region was increased with increasing downstream location, θ, to account for the growth of the structures and was equivalent on the average to $\Delta z \approx 6 y_2$. The velocity vectors overlaid on top of the contours represent the sum of the stationary and coherent (thereafter referred to as S&C) ensemble averaged velocity vectors in the yz-plane (with the exception of figure 12). The profiles in the accompanying figures represent chosen cross sections through the counter-rotating vortices and between them as well as the spanwise averaged constituent of the quantity considered.

Figure 11(a) represents contours of ensemble averaged streamwise vorticity $\langle \omega_x \rangle$ wile the velocity vectors plotted superimposed on it represent the sum of the stationary mean radial velocity, $\bar{v}/U_{max}$, and the radial velocity induced by the streamwise vortices, $\tilde{v}$. The sign of the latter depends on its spanwise location relative to a particular vortex core and it is capable of overwhelming $\bar{v}/U_{max}$ in the downwash region between the two vortices (marked by λ in figure 11). To the left of the vortex rotating in a counter clockwise direction (i.e. containing $\langle \omega_x \rangle > 0$), the downwash flow (where $\bar{v}/U_{max} < 0$) is brought to stagnation around $y/y_2 = 0.3$ while to the right of it, it stops only at $y/y_2 = 1.3$ (figure 11b). This is because the vortex-induced-flow changes its direction along the span while the mean outflow and inflow in the wall and outer regions respectively are almost constant at all spanwise locations. Since the core of the average streamwise vortices is located at $y/y_2 = 0.75$, the interaction between the streamwise vortices and the mean flow is biased toward the inner region where $y/y_2 \leq 1$.

The purely coherent constituent of this flow is obtained by subtracting the stationary component $\bar{v}/U_{max}$ obtained by the simple averaging of the PIV data. Consequently, the spanwise-averaged coherent part of the radial velocity component, $\tilde{v}$, must vanish everywhere across the jet and it actually does so (figure 12b). Other plots of $\tilde{v}$ across the cores of the vortices resemble the classical velocity distributions in a Rankine vortex that are dominated by a solid-body rotation within the core and a potential flow far from it.

In section 4 (figure 10) we presented the mean and fluctuating components of the cross flow velocities obtained by conventional double decomposition. This presentation lumped all the non-stationary data into one turbulent constituent. Therefore, double decomposition is not capable of distinguishing between typically random turbulence and the undulating, unsteady, yet coherent flow (e.g. the longitudinal counter rotating structures discussed above). For example, because the mean velocities induced by the streamwise vortices change sign across each vortex the meander of these vortices results in a temporal variation of the local velocity field that contributes to the time dependent component i.e. turbulence. In other words, vortices that are sufficiently unsteady so as not to cause spanwise variation in the mean flow simply contribute to the Reynolds stresses in the double decomposition (DD). For this reason, the turbulence intensities $\sqrt{\overline{v'^2}}/U_{max}\Big|_{DD}$ and $\sqrt{\overline{w'^2}}/U_{max}\Big|_{DD}$ attain excessive values in a spatially fixed coordinate system. If the data are to be decomposed into three constituents (stationary, coherent, and random), the random turbulence intensities, $\sqrt{\overline{v'^2}}/U_{max}\Big|_{STD}$ and $\sqrt{\overline{w'^2}}/U_{max}\Big|_{STD}$, averaged along the span must be lower in comparison (figures 13b and 14b). The difference between the maxima obtained by the two methods of decomposition (DD & STD) is approximately 25% for both velocity components.

The highest intensity of the random, $\sqrt{\overline{v'^2}}/U_{max}\Big|_{STD}$ fluctuations measured relative to the core of the streamwise vortices occurs between the counter rotating pair of vortices that eject fluid from the surface outward (figure 13(a) $y/y_2 = 0.9$; $z/y_2 = \pm 1$), while the zone

between the pair of vortices that transport fluid toward the surface contains a significantly lower level of random $\sqrt{\overline{v'^2}}/U_{max}\Big|_{STD}$ fluctuations ($z/y_2 = 0$). The core of the streamwise vortices is rather quiescent regardless of the sign of their rotation. This suggests that differences among the individual vortices in terms of size and intensity contribute to $\sqrt{\overline{v'^2}}/U_{max}\Big|_{STD}$. The selective location of the maximum in $\sqrt{\overline{v'^2}}/U_{max}\Big|_{STD}$ implies that the highest velocity fluid (that resides in the mean around $y/y_2 = 0.2$) is pushed outward by the streamwise vortices increasing the local rate of strain at $0.5 < y/y_2 < 1$ and thus turbulence production at this height above the surface. A similar correlation exists between the spanwise component of random fluctuations w' and the large streamwise vortices. The distribution of the secondary shear stress $\overline{v'w'}/U^2_{max}\Big|_{STD}$ is not presented because of its extremely low levels. The intensity profiles shown in figures 13(b) & 14(b) represent a cross section through a core of the vortex and in the up-wash region between two vortices.

6. The Longitudinal Structures

Thus far, we have provided evidence for the presence of streamwise vortices in the turbulent curved wall jet. The next step is it to analyze their development in the direction of streaming and assess their size and strength. The best characterization of a vortex is by its circulation, Γ. If it is not altered by a specific mechanism, it should remain approximately constant throughout the flow. The circulation was determined by evaluating the surface integral of the streamwise vorticity field ω_x. Vorticity values lower than 20% of the maximum were set to zero in order to reduce the influence of noise. Even at downstream locations where the structures were relatively weak, this method provided stable and consistent results. Several convergence tests showed that the average of individual sub-samples (one third of the whole data record) agreed to within 5% with the result of the total record. Clockwise and counter-clockwise rotating vortices were averaged separately.

Four experiments were conducted at equally spaced downstream locations, ranging from $\theta = 40°$ to $160°$. The results for both signs of the streamwise circulation $\pm\Gamma_x$ are given in figure 15 using two definitions: (i) is the streamwise circulation per wavelength $\pm\Gamma_{x,\lambda}$ and (ii) is the streamwise circulation per unit span $\pm\Gamma_{x,\Delta z}$. The circulation per unit span $\pm\Gamma_{x,\Delta z}$ (labeled by open squares) stays approximately constant with increasing distance from the nozzle whereas the circulation per wavelength is approximately doubled every $\Delta\theta = 40°$ (solid circles). A possible explanation for this increase is an amalgamation of vortices having the same sign. Consequently, the scale of the structures, but not their strength, increases proportionally to the width of the flow. This implies that the vortices observed are not amplified in the linear sense, but they do so due to vortex amalgamations that may represent a secondary instability. Earlier findings using cross-correlation measurements that (Likhachev, Neuendorf & Wygnanski) that were confirmed by the present PIV data (figure 16) support this notion. The results show that

the spacing of the streamwise structures grows proportionally to the jet width. For the PIV data the mean spanwise spacing was calculated by dividing the span interrogated by the average number of the vortices identified.

The increase of the streamwise circulation $\pm\Gamma_{x,\lambda}$ and the increase in λ_z with increasing distance from the nozzle is continuous (figures 15 and 16). This is in contrary to Plesniak's et al. (1994) observation that was made in a curved turbulent mixing layer. They describe a step-wise increase in spacing and in circulation. Such a behavior is known from mixing layers at low Reynolds number (Moser and Rogers, 1993). In fully turbulent flows a smooth development is more likely to occur due to the meander of the structures and due to their variation in size and strength. In other words, in a fully turbulent flow (without external excitation), amalgamation of coherent structures can occur at any location and at any time. A regular and repeatable amalgamation of streamwise vortices is unlikely in a fully turbulent flow because clusters of positive and negative vorticity appear irregularly in space and time. Therefore, the vortices illustrated in figure 12 represents an average only.

More contours of the coherent streamwise structures measured at $\theta = 40°$, $80°$, $120°$, and $160°$ are not plotted because they reveal little novel information. It is worth mentioning that the average distance of the vortex cores from the surface increases from $0.7y_2$ at $\theta = 80°$ to approximately 1 at $\theta = 120°$. This suggests that the vortex cores get squeezed out due to their growth in the fixed span experiment or they rotate outward with increasing distance in the direction of streaming. This rotation might be caused by the maximum velocity located at $y/y_2 \leq 0.2$, that advects the vorticity near the surface faster downstream than the vorticity that is away from it. Such rotation of the streamwise vortices, if proven correct, would contribute to Ω_y that might lead to the proposed cellular separation of the flow. The $\theta = 120°$ location coincides with the beginning of the adverse surface pressure region that leads to the eventual separation of the wall jet (see N&W).

7. Some Preliminary Effects of Two - Dimensional Excitation

When the flow emanating from the slot was excited in a two dimensional, harmonic manner, it triggered large spanwise eddies that crossed periodically a given streamwise location. Furthermore the forced input provided the phase reference (i.e. trigger input to the laser) required for phase averaging the data. This enabled one to examine the effect of periodic excitation on the large spanwise and streamwise vortices coexisting simultaneously in the flow. The distribution of spanwise vorticity and streamwise velocity over the cylinder are provided by illuminating the flow in the (R,θ) plane. Four phase-locked and ensemble averaged spanwise vorticity contours, $\langle \omega_z \rangle$, are plotted in figure 17, together with the corresponding velocity profiles $\langle u \rangle / U_{max}$ measured at $\theta = 80°$. They are separated by a phase difference of $\Delta\phi = \pi/2$. The mean velocity profile is plotted on the same figures for comparison. The maximum velocities at $\phi = 0$ and π are approximately the same and they are equal to the mean maximum velocity, U_{max}. The streamlines that are superposed on the vorticity contours, converge toward the surface at

$\phi = 0$ and they diverge away from the surface at $\phi = \pi$. The flow accelerates between $\phi = \pi/2$ and $\phi = 3\pi/2$ increasing the rate of strain during this half of the forcing cycle and with it the absolute values of $\|\langle\omega_z\rangle\|$ near the surface and in the outer region. The flow decelerates during the other half of the cycle with opposite effects on $\|\langle\omega_z\rangle\|$.

Illumination in the cross plane at $\theta = 80^\circ$ provided phase locked data for the streamwise vortices discussed earlier. When these PIV results were processed through the pattern recognition and alignment procedure, regular arrays of counter rotating vortices emerged. Their contour plots are not shown because they do not differ from those plots shown in figures 11 through 14. At first sight the streamwise vortices appear to oscillate up and down at the frequency of excitation changing their core location from a minimum of $y_{core}/y_2 = 0.55$ occurring at $\phi = 0$ to $y_{core}/y_2 = 0.8$ corresponding to $\phi = \pi$ (figure 18). This correlates well with the divergence or convergence of the streamlines in the outer part of the wall jet where the cores of the streamwise vortices reside. Calculating the circulation in these streamwise vortices Γ_x per spanwise wavelength revealed that the latter is tied to the acceleration within the wall jet and has similar behavior to the maximum velocity (figure 18).

An example of the phase averaged streamwise vorticity is plotted in figure 19. The phase selected was, $5\pi/4$ because then the large spanwise eddy just rolled over the illuminated plane at $\theta = 80^\circ$. This stretched and regulated the streamwise vortices that became apparent even in the absence of pattern recognition. Although the perceived intensity of the ensemble-averaged vortices is weaker and they seem to be stretched in the vertical direction, they provide clear evidence to the spanwise inhomogeneity in the flow. The weakness of the ensemble averaged contours stems in part from the dispersion in height of the various vortices relative to the surface. The histogram of vortex core locations above the surface is also show in figure 19b suggesting that the mean location of the streamwise eddies is around y/y$_2$=0.7. The meandering of the streamwise vortices along the span is not stopped by the excitation since their preferred spanwise location changes depending on the phase at which the data was taken. Thus in the mean even the forced flow remains two-dimensional.

8. Summary and Conclusions

PIV measurements undertaken at several cross-sectional planes, ranging from $\theta = 40^\circ$ to 160° revealed the existence of counter rotating vortex pairs in a wall jet flowing over a circular cylinder. Pattern recognition techniques had to be used in order to describe these vortices in a statistical manner and to separate the data into stationary, coherent, and random constituents. Freed from the high frequency background turbulence and their own low frequency meander, the vortices mapped provided a new insight into the effects of curvature and possibly centrifugal instability in highly turbulent shear flows. The results suggest that the longitudinal structures are not stationary and thus do not to contribute to mean spanwise distortions, but they are strong enough to augment the Reynolds stresses and thus increase the rate of spread of the flow and its turbulent intensities. Their spanwise wavelength λ_z, might have determined the width of the jet as it was found to

scale with the local width y_2, providing the relationship $\lambda_z \approx 2y_2$. Finally, the circulation of the individual structures $\Gamma_{x,\lambda}$ doubled every $\Delta\theta = 40°$, yet their number per unit span halved in each interval leaving the circulation per unit span $\Gamma_{x,\Delta z}$ as being approximately constant. This would suggest that the vortices are increasing their strength through amalgamation and not through amplification, implying that even a weakly non-linear stability approach to their development may be wrong. Also the interaction between streamwise vortices and the spanwise ones, generated by a Kelvin-Helmholtz instability that was enhanced by periodic excitation, was not simple though it decreased the meandering of the former along the span. This interaction might be used in the future as a diagnostic tool in conjunction with a three component PIV capable of resolving the streamwise and spanwise flow for the same realization.

9. References

BLACKWELDER, R.F. and KAPLAN, R.E., 1972: "The intermittent structure of the wall region in a turbulent boundary layer". Proc. of the 12th IUTAM International Congress of Applied Mechanics Moscow

BRADSHAW, P. 1969 Effects of streamline curvature on turbulent flow. *AGARDograph* **169**.

FEKETE, G.I. 1963 Coanda flow of a two-dimensional wall jet on the outside of a cylinder. Dept. of Mech. Eng., *Rep.* 63-11, McGill University.

GASTER, M., KIT, E. and WYGNANSKI, I., 1985 "Large-scale strictures in a forced turbulent mixing layer", *J. of Fluid Mech.*, **150**, 23-39.

GUITTON, D.E. 1970 Some contributions to the study of equilibrium and non equilibrium turbulent wall jets over curved surfaces. PhD. Thesis Dept. of Mech. Eng., McGill University.

HUSSAIN, A.K.M.F. 1983 Coherent structures - reality and myth. *Phys. Fluids* **26**, 2816.

KROTHAPALLI, A., RAJKUPERAN, E., ALVI, F. & LOURENCO, L. 1999 Flow field and noise characteristics of a supersonic impinging jet. *J. Fluid Mech.* **392**, 155-181.

LIKHACHEV, O., NEUENDORF, R. & WYGNANSKI, I. 2001, On streamwise vortices in a turbulent wall jet that flows over a convex surface. *Phys Fluids.* **13**, 1822-1825

LOURENCO, L. & KROTHAPALLI, A. 1998 Mesh-free second order accurate algorithm for PIV processing. *PROC. Intl. Conf. On Optical Technology and Image Processing in Fluid, Thermal and Combustion Flows, Yokohama, Japan, December 1998*, 224

MARGOLIS, D.R. & LUMLEY, J.L. 1965 Curved turbulent mixing layer. *Phys. Fluids* **8**, 1775-1784

MATSSON, O.J.E. 1995 Experiment on streamwise vortices in curved wall jet flow. *Phys. Fluids* **8**, 2978-2988.

NEUENDORF, R. & WYGNANSKI, I. 1999 On a turbulent wall jet flowing over a circular cylinder. *Jour. Fluid Mech.* **381**, 1-25

OSTER, D., WYGNANSKI, I., DZIOMBA, B., FIEDLER, H., 1978 "The Effect of Initial Conditions on the Two-Dimensional ,turbulent Mixing Layer" in Structure and Mechanics of Turbulence, H. Fiedler ed. (Lecture Notes in Physics vol. 75, 48) Springer-Verlag, Berlin.

PATEL, V.C. & SOTIROPOULUS F.,1997, Longitudinal curvature effects in turbulent boundary layers. , *Prog. Aerospace Sc.* **33**, 1-70.

PLESNIAK, M.W., MEHTA, R.D. & JOHNSTON, J.P. 1994 Curved two-stream turbulent mixing layers: three-dimensional structure and streamwise evolution. *J. Fluid Mech.* **270**, 1-50.

SARIC, W.S., 1994 "Gortler vortices" *Annu. Rev.Fluid Mech.* **26, 379-409.**

SCHUBAUER, G. B. and SKRAMSTAD, H. K., 1948 "Laminar Boundary Layer Oscillations and Transition on a Flat Pate" NACA Rep 909,.

TANI, I., 1962: Production of longitudinal vortices in the boundary layer along a concave wall, *J. Geophys. Res.* **67**, 3075-3081.

TOWNSEND, A.A., 1956,1973 *"The structure of turbulent shear flows"* Cambridge University Press, London

WYNGAARD, J.C., TENNEKES, H., LUMLEY, J.L. & MARGOLIS, D.P. 1968 Structure of Turbulence in a Curved Mixing Layer. *Phys. Fluids* **11-6**, 1251-1253.

ZHOU, M.D., HEINE, Chr. & WYGNANSKI, I. 1996 The effect of excitation on the coherent and random motion in a plane wall jet. *J. Fluid Mech.* **310**, 1-37.
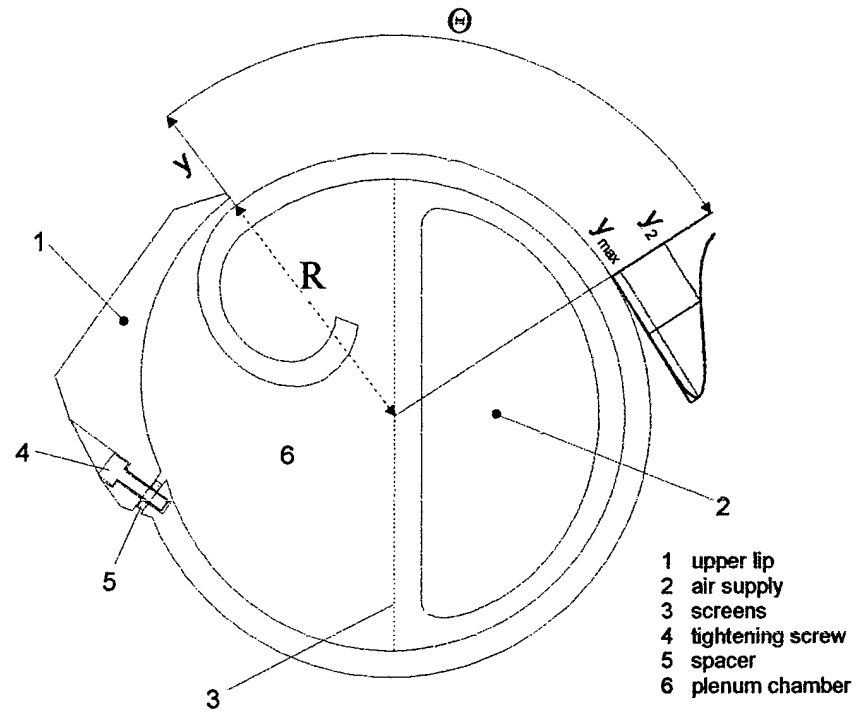
Figure 1 A cross section of the experimental facility

1 upper lip
2 air supply
3 screens
4 tightening screw
5 spacer
6 plenum chamber
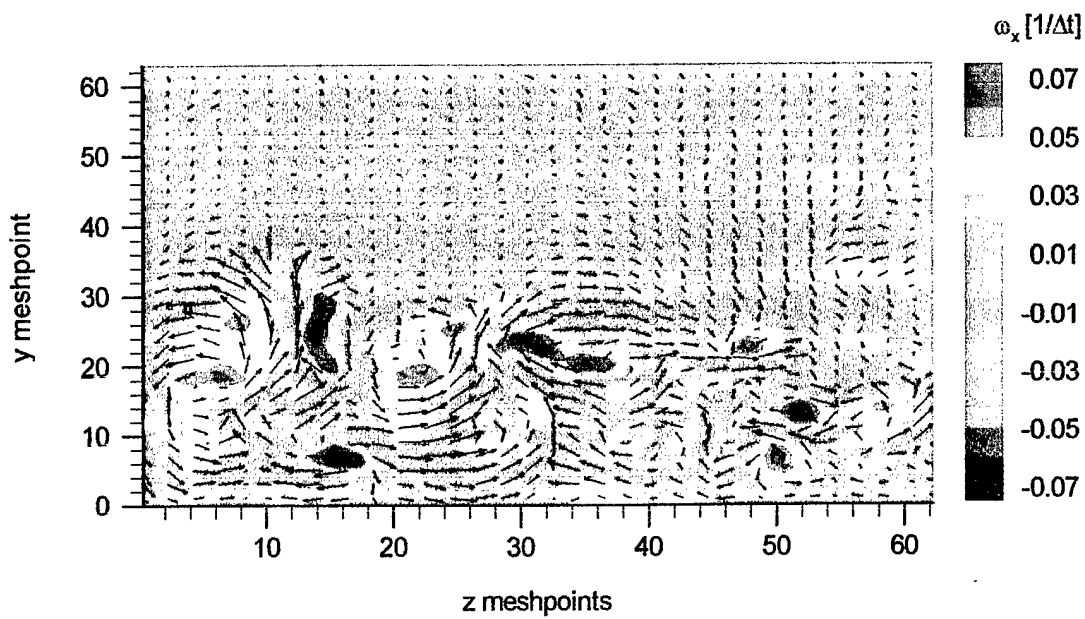
Figure 2: Vorticity contours of an instantaneous PIV image ω_x (y,z)
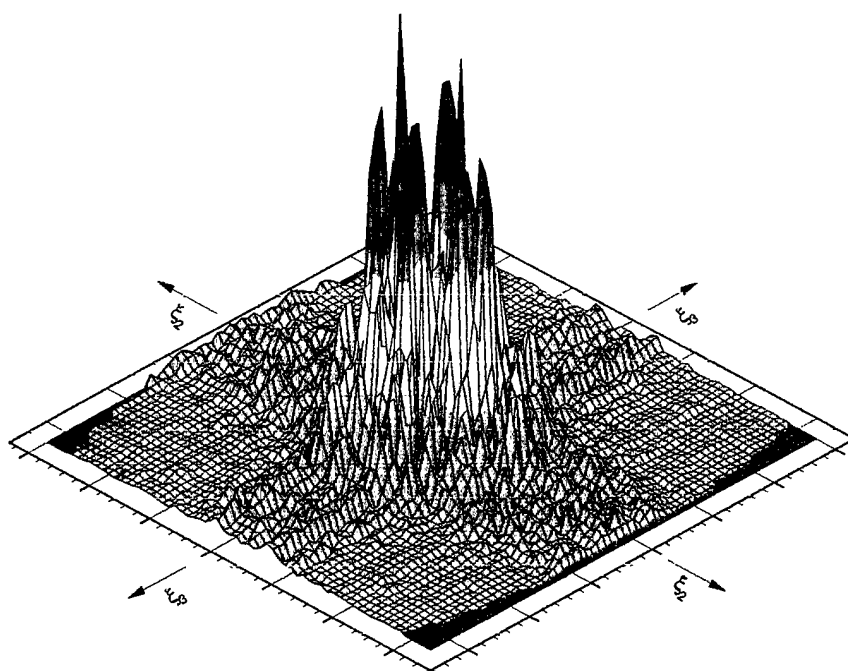
Figure 3: Fourier Transformation $F(\zeta_2, \zeta_3)$ of the instantaneous PIV image ω_x (y,z)
(see figure 2)

3.

Figure 4: Amplitude of the Fourier transformation $F(\zeta_2, \zeta_3)$ for positive ζ_3 and $\zeta_2 = 0$

(b)
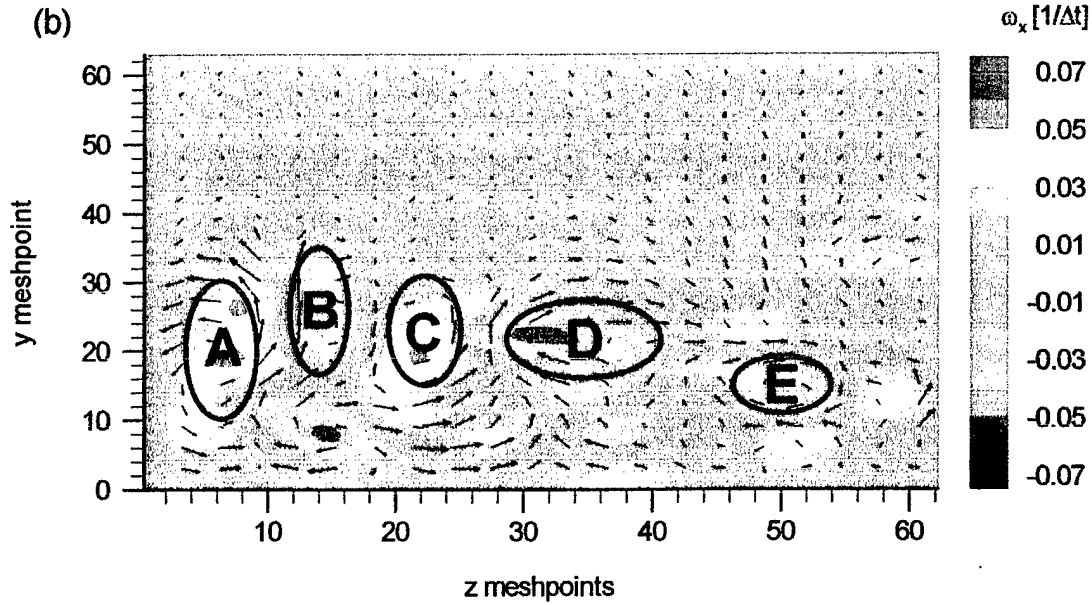
Figure 5: Low-pass filtered vorticity contours of an instantaneous PIV image $\omega_x(y,z)$ (see figure 2)
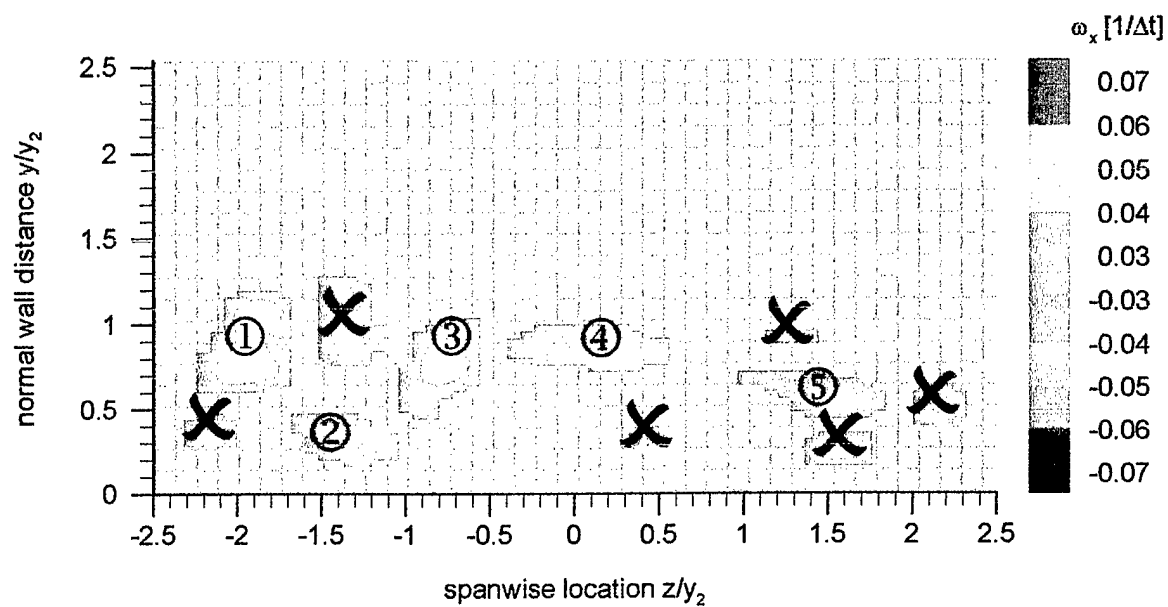
Figure 6: Low-pass filtered and threshold clipped vorticity (contours of an instantaneous PIV image $\omega_x(y,z)$ (see also figure 2 and 5))
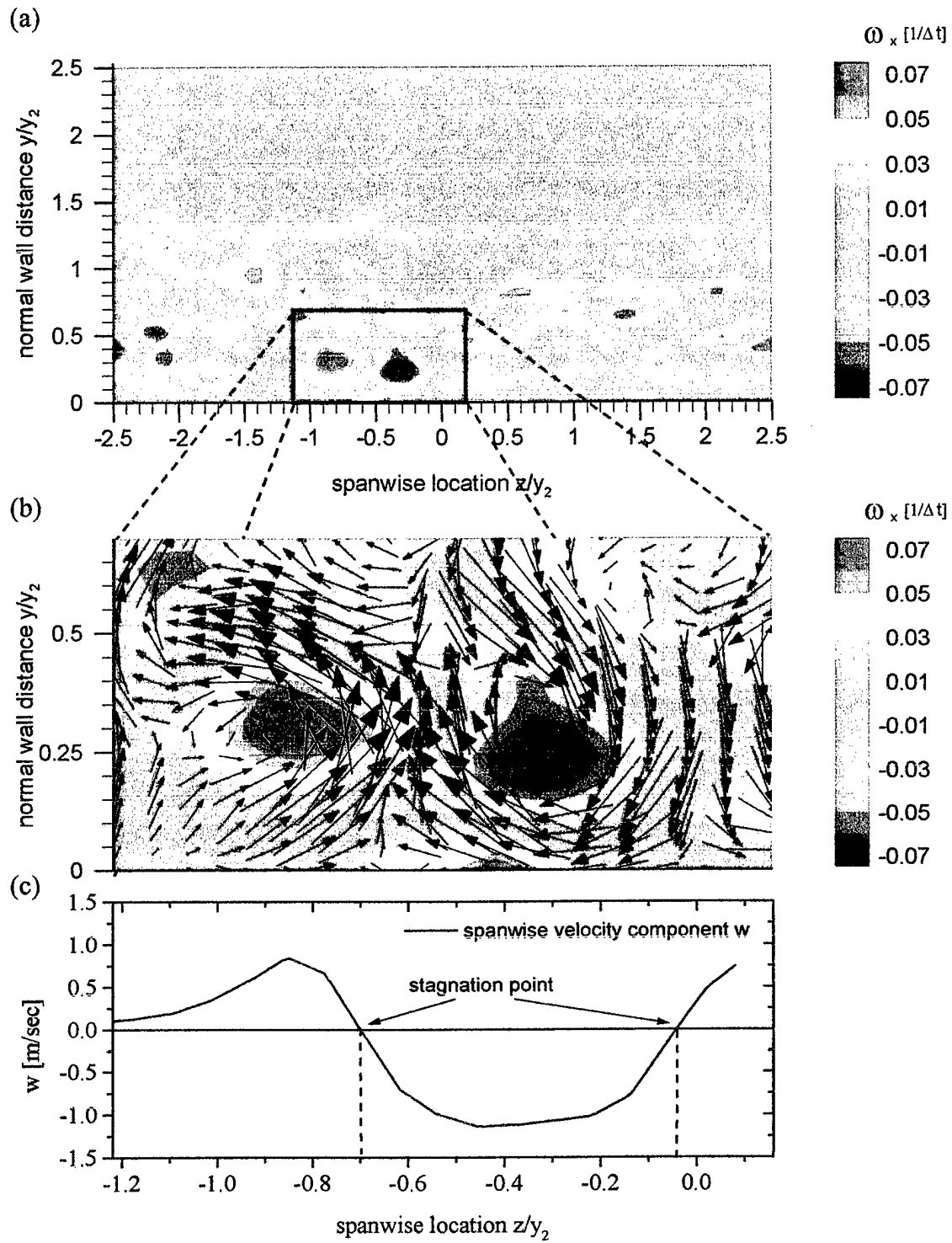
Figure 7: (a) & (b) Vorticity contours of an instantaneous PIV image ω_x (y,z). (c) Spanwise distribution of the spanwise velocity component w in the vicinity of the surface (y/$y_2 \approx$ 0).

(d)
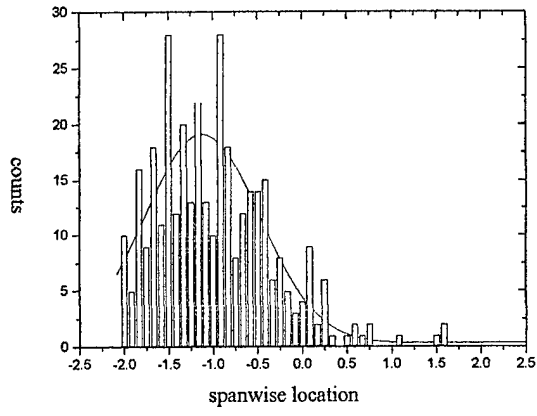
(e)
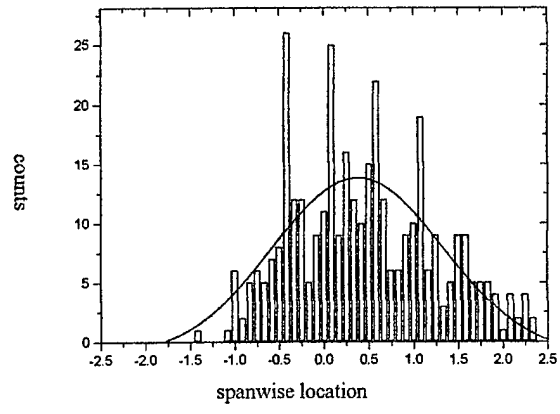
(f)
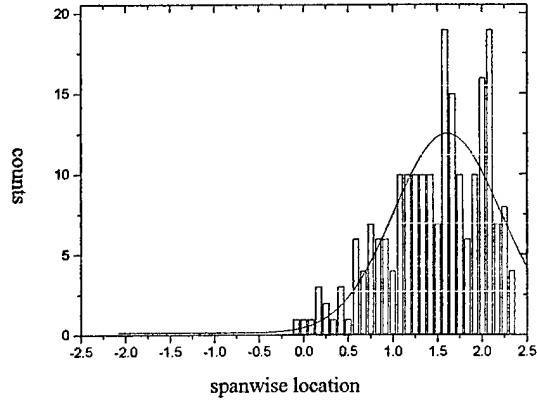
(g)
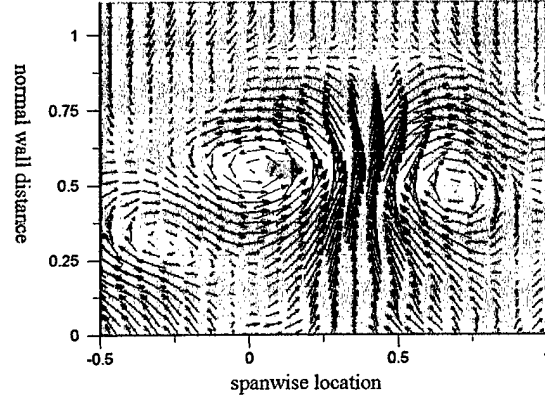
Figure 7: Histograms of the spanwise location z/y_2 of the zero crossings of the spanwise velocity component w. (d) 1st, (e) 2nd, and (f) 3rd vortex pair. (g) Image of the 2nd vortex pair

Figure 8: (a) Contours of streamwise mean vorticity $\Omega_x\, y_2/U_{max}$ and (b) the corresponding spanwise averaged radial velocity component $\bar{v}/U_{max}$ at the downstream location $\theta = 80°$.

Figure 9: A comparison of hot-wire and PIV measurements at the downstream
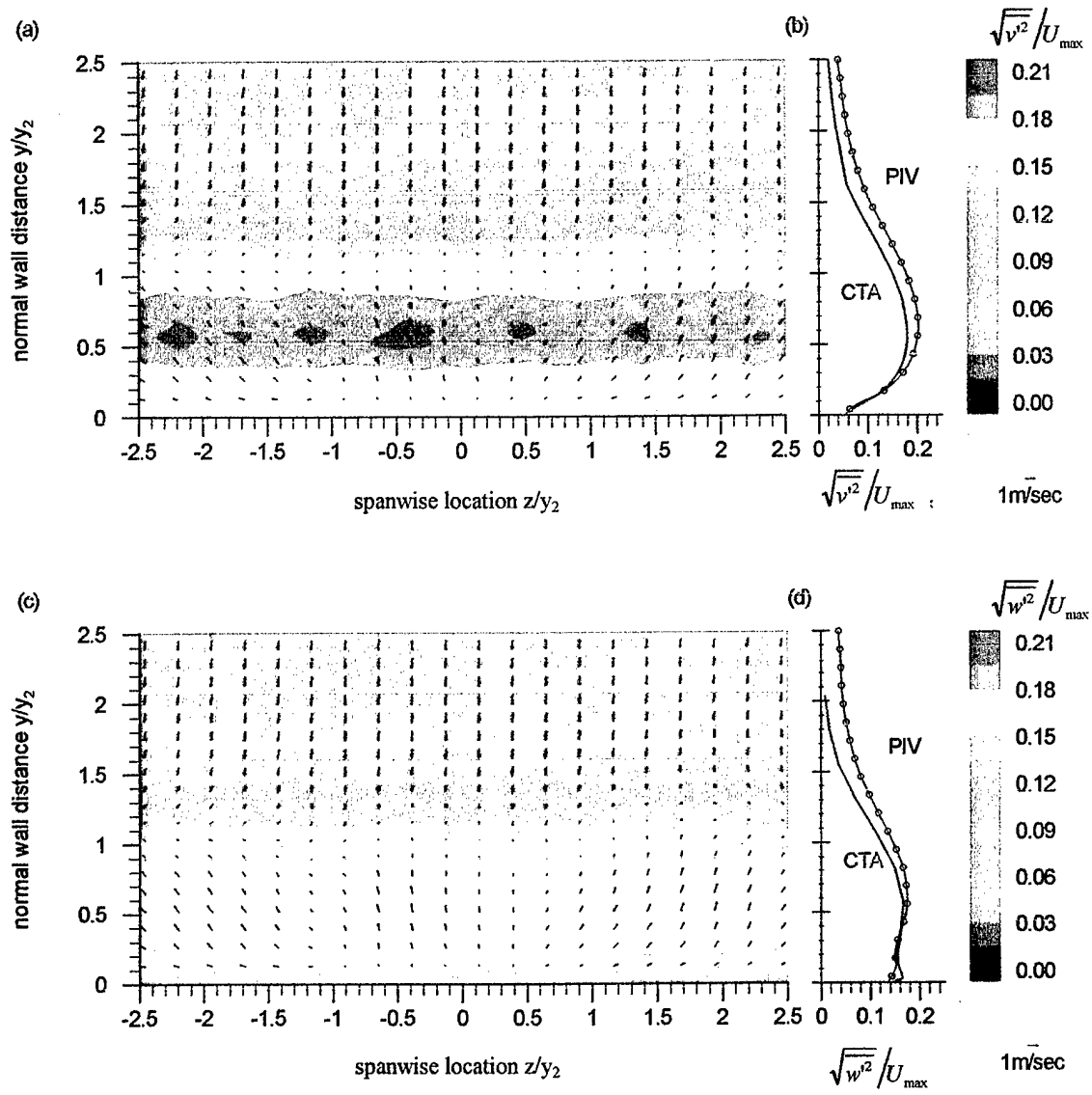
Figure 10: (a), (c) Turbulence intensity contours of the transverse Reynolds stresses $\sqrt{\langle v'^2 \rangle}/U_{max}$ and $\sqrt{\langle w'^2 \rangle}/U_{max}$ and (b), (d) the corresponding spanwise averaged turbulence intensity profiles at the downstream location $\theta = 80°$.
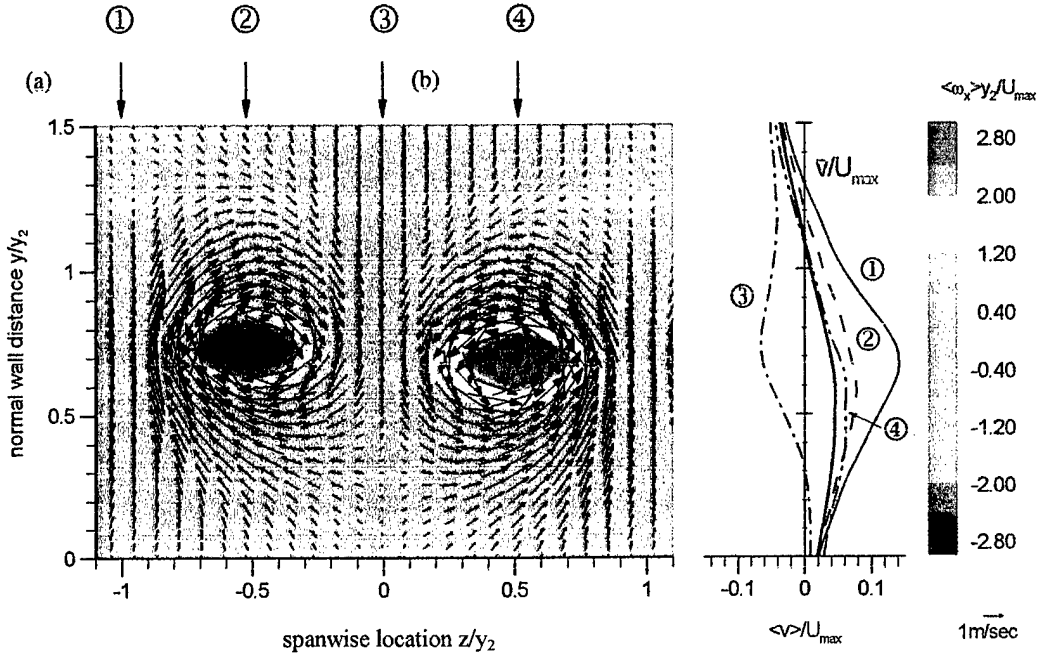
Figure 11: (a) Contours of phase averaged streamwise vorticity $\langle \omega_x \rangle y_2 / U_{max}$ and (b) the corresponding profiles of the spanwise averaged radial velocity component $\bar{v}/U_{max}$ at the downstream location $\theta = 80°$. The profiles ① through ④ represent the phase averaged radial velocity components $\langle v \rangle / U_{max}$ at the cross sections $z/y_2 = -1, 0.5, 0, \text{ and } 0.5$, respectively.
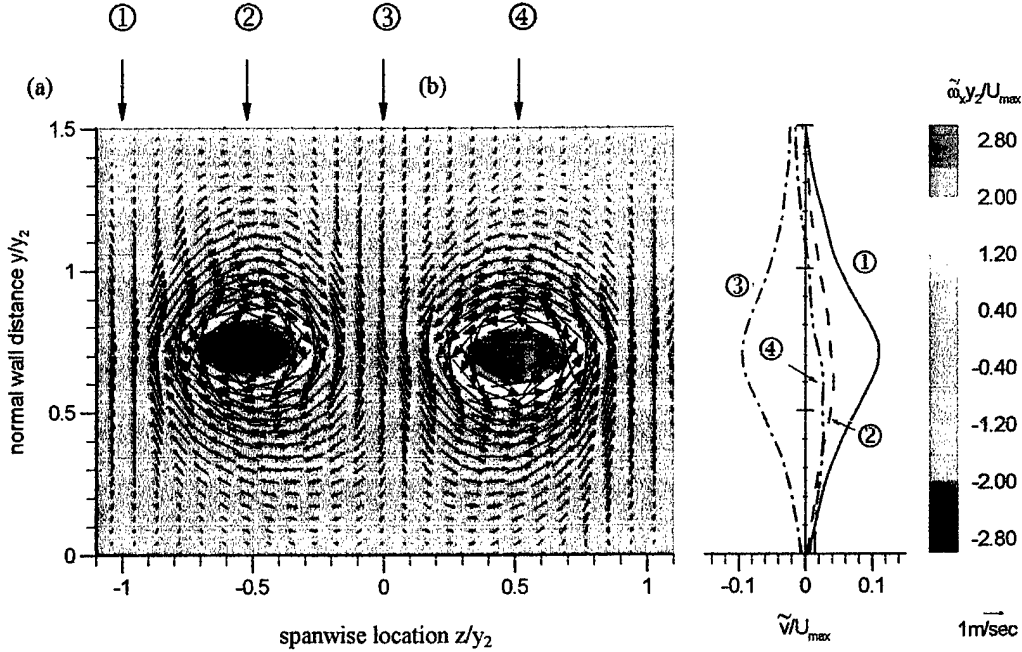
Figure 12: (a) Contours of coherent streamwise vorticity $\tilde{\omega}_x y_2 / U_{max}$ at the downstream location $\theta = 80°$. The profiles ① and ④ represent the phase averaged coherent radial velocity components $\tilde{v}/U_{max}$ at the cross sections $z/y_2 = -1, 0.5, 0, \text{ and } 0.5$, respectively.

26
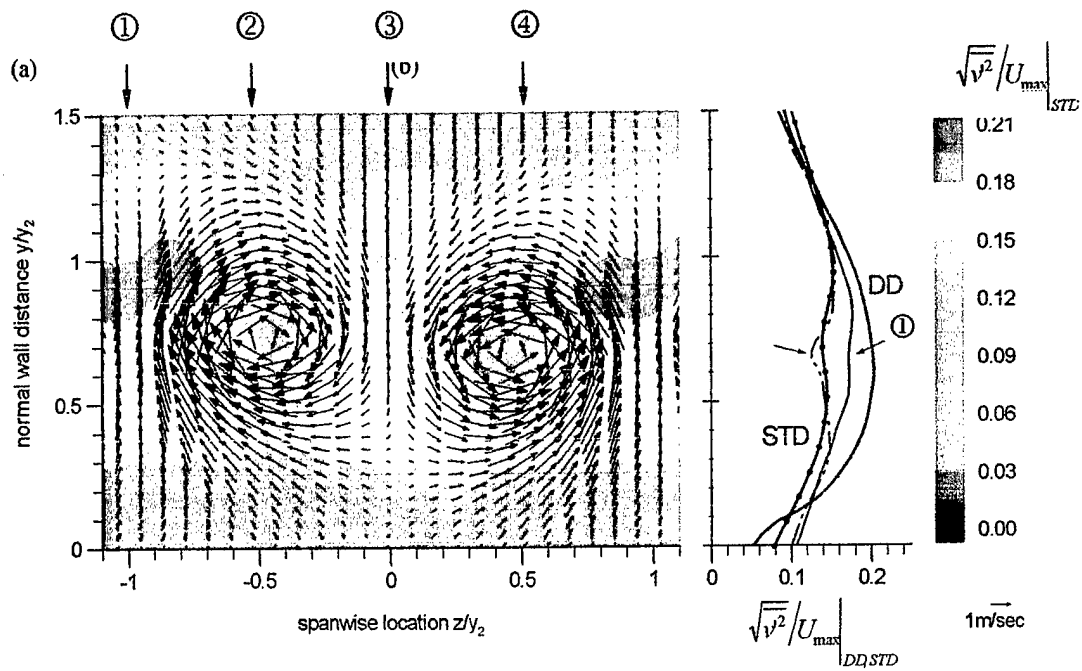
Figure 13: (a) Contours of the radial turbulence intensity component $\sqrt{v'^2}\big/U_{max}\big|_{STD}$ for STD and (b) comparison of the corresponding spanwise averaged turbulence intensity profiles for STD and DD at the downstream location $\theta = 80°$. The profiles ① and ④ represent the turbulence intensities for STD at the cross section $z/y_2 = -1$ and 0.5.
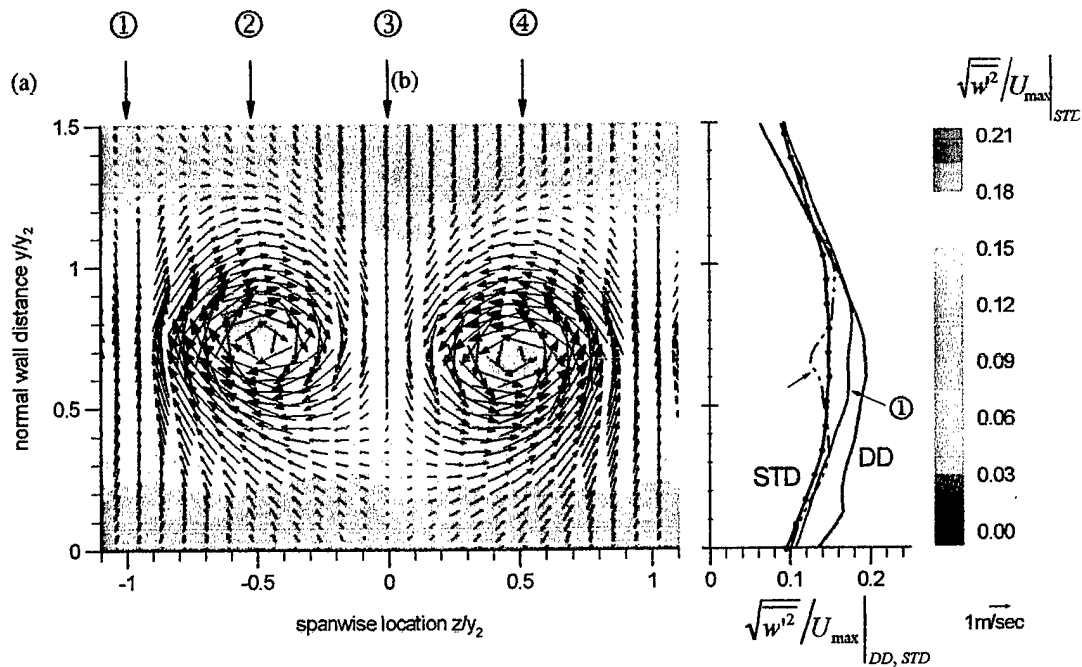
Figure 14: (a) Contours of the radial turbulence intensity component $\sqrt{w'^2}\big/U_{max}\big|_{STD}$ for STD and (b) comparison of the corresponding spanwise averaged turbulence intensity profiles for STD and DD at the downstream location $\theta = 80°$. The profiles ① and ④ represent the turbulence intensities for STD at the cross section $z/y_2 = -1$ and 0.5.
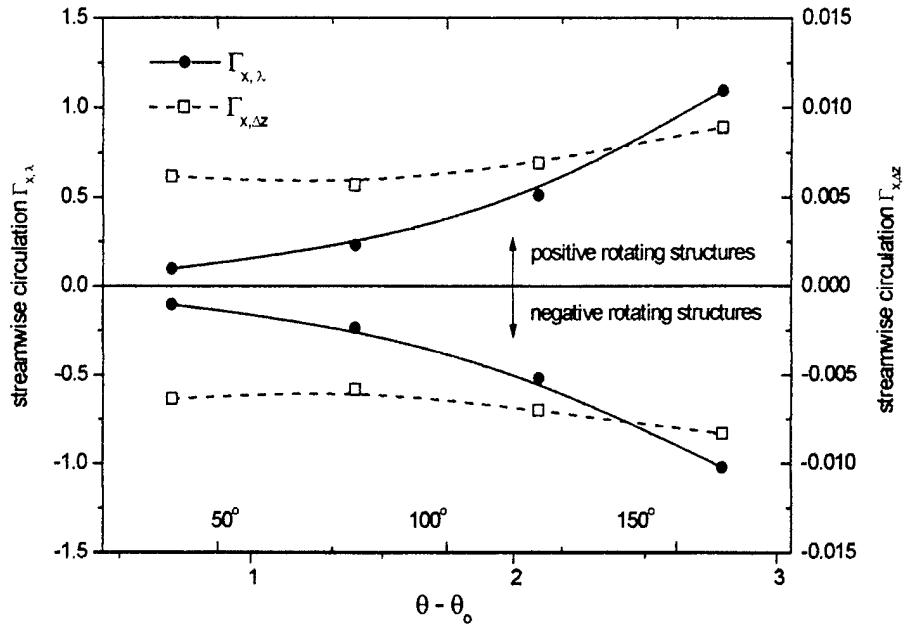
Figure 15: The development of the streamwise component of circulation Γ_x in the direction of streaming.
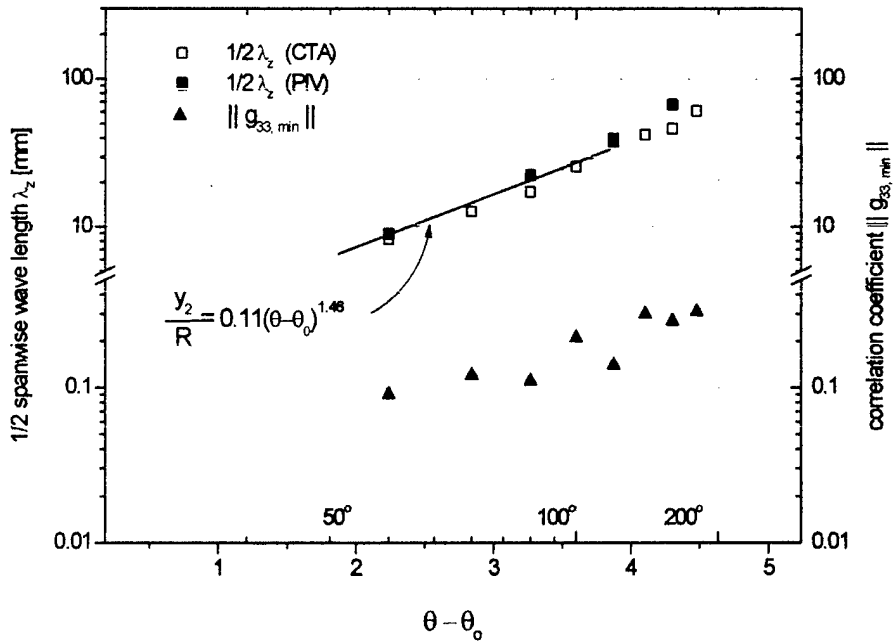
Figure 16: The development of the spanwise wave length λ_z and the minimum correlation Coefficient g_{33} in the direction of streaming.

28
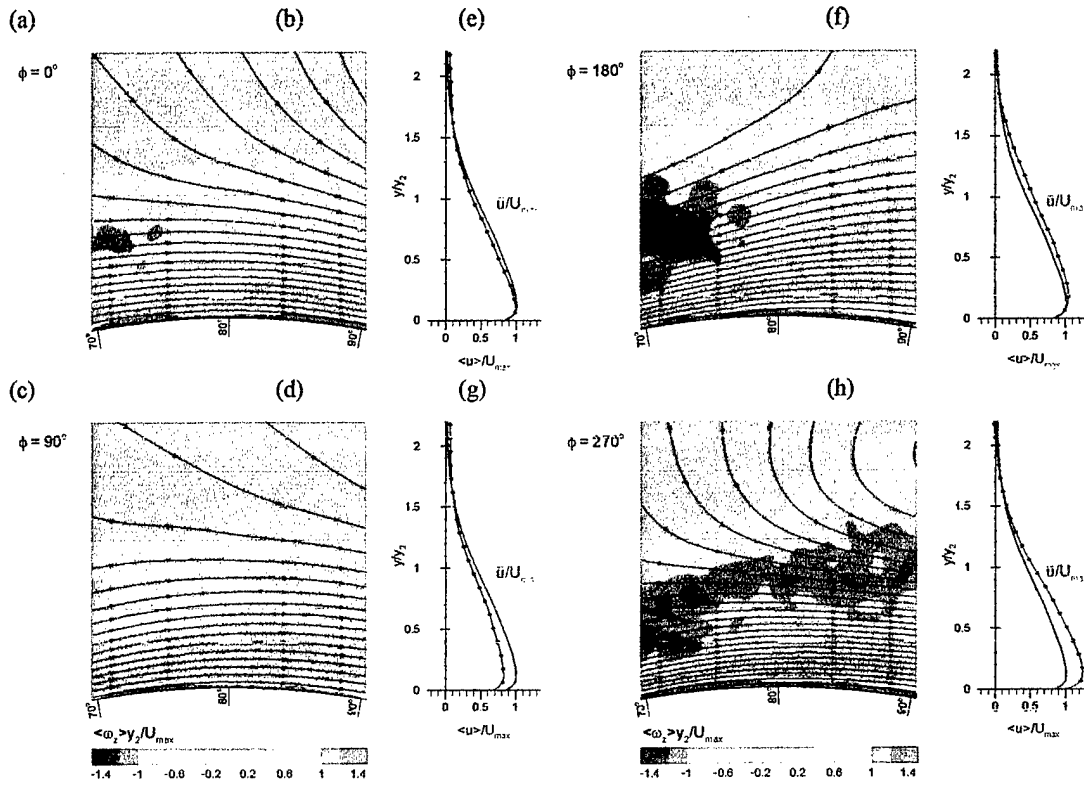
Figure 17: (a), (c), (e), and (g) Sequence of phase averaged spanwise vorticity contours $\langle\omega_z\rangle y_2/U_{max}$ and (b), (d), (f), and (h) the corresponding profiles of the spanwise averaged radial velocity component $\langle u\rangle/U_{max}$ at the downstream location $\theta = 80°$ for $\phi = 0$, $\frac{1}{2}\pi$, π, and $\frac{3}{4}\pi$.
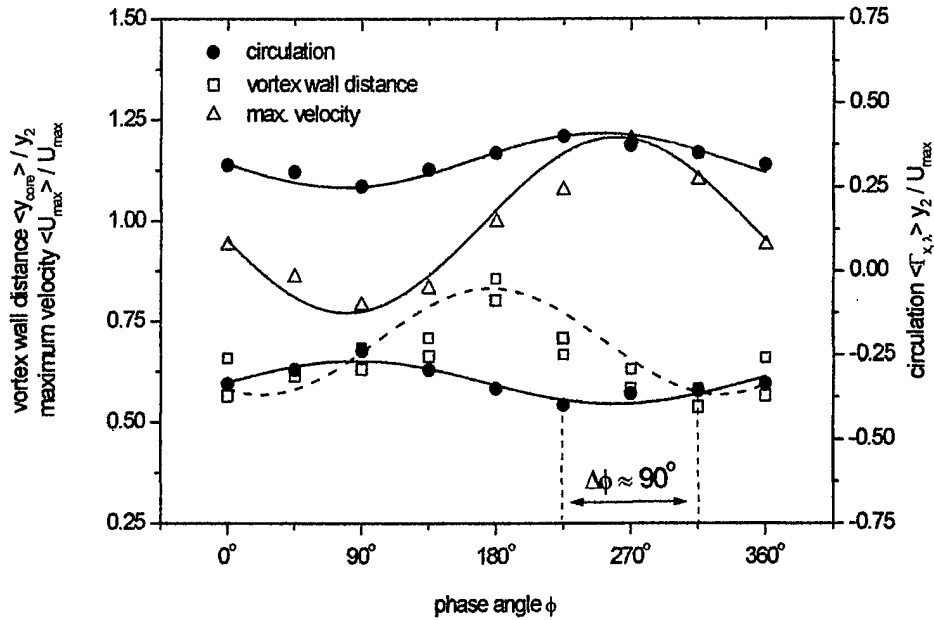
Figure 18: The development of the phase averaged vortex wall distance $\langle y_{core}\rangle/y_2$, the maximum phase average velocity $\langle u\rangle_{max}/U_{max}$ and the circulation $\Gamma_{x\lambda}$ with ϕ.
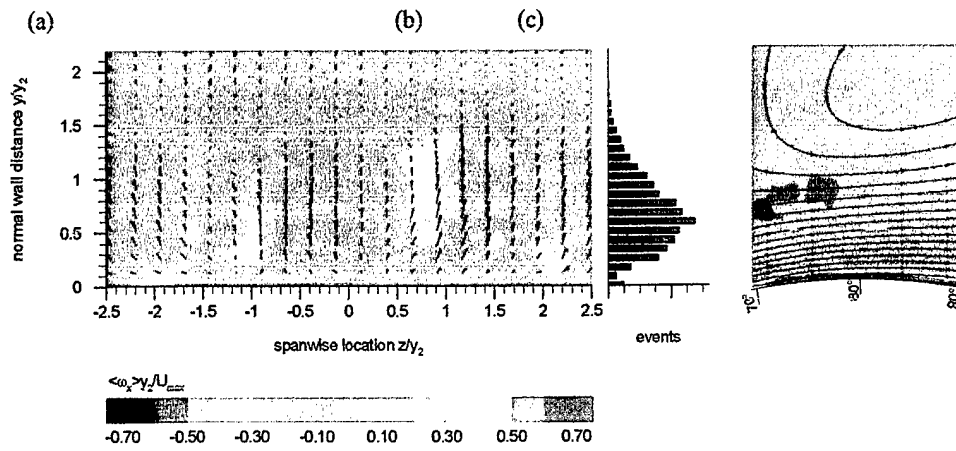
Figure 19: (a) Contours of phase averaged streamwise vorticity $\langle \omega_x \rangle y_2 / U_{max}$, (b) core location probability distribution $\langle y_{core} \rangle / y_2$, and (c) contours of phase averaged spanwise vorticity $\langle \omega_z \rangle y_2 / U_{max}$ for $\phi = 5/4\pi$ at the downstream location $\theta = 80°$ (without pattern recognition).

THE EFFECT OF MASSLESS JET ON A FLOW AROUND A CIRCULAR CYLINDER

Abstract

The parameters governing forced attachment of flow to a flat, inclined surface, were determined by Nishri[1]. The addition of convex curvature is investigated presently using the circular cylinder as a model. In both flows the forcing consisted of two-dimensional, periodic oscillations emanating from a narrow slot. Naturally the flow separates from the surface of a smooth circular cylinder around 70° from the leading stagnation point when the Reynolds number is approximately 40,000.

Periodic excitation from a slot located some 40° further downstream from the natural separation location altered very significantly the pressure distribution on that surface. On the opposite side of the cylinder neither the location of separation on the opposite side nor the pressure distribution was substantially affected, but a major change in the base pressure was observed. The cylinder started to lift and the typical vortex shedding from the cylinder was altered if not entirely eliminated. Experiments were carried out using both pressure measurements and particle image velocimetry (PIV). Numerical simulations were also carried out using an unstructured mesh finite element method with dynamic and constant coefficient Smagorinsky large eddy simulation (LES) turbulence models.

1. Introduction

Bluff Bodies are found in numerous technical applications. In some of these it is preferable to control the drag and/or lift to either adapt the flow to variable conditions or to optimize it for a given situation.

This case is found widely at the tail of fast moving bodies, for example airplanes or helicopters. Various attempts are being made to prevent the drag penalty that is related to conventional solutions by application of active flow control.

A cylinder was chosen to fundamentally investigate the vortex shedding from a bluff body and its control by periodic excitation. Furthermore the influence of a convex surface on separation and reattachment is of interest. The experiments were carried out in the sub critical range at a Reynolds number of 36,000. In this range, the drag is relatively Reynolds number independent. This allows the investigation of the shedding of a laminar boundary layer as the most basic case. Therefore, no attempt was made to control the separation by affecting the transition of the boundary layer to turbulence, like investigated by Naim[2]. In this stage of the experiments only sinusoidal 2-D excitation has been applied as the simplest case of periodic forcing. For future work internal excitation will be used which includes the possibility of spanwise variation of the excitation. This is necessary to investigate the influence of streamwise structures formed by periodic excitation on the separation on a convex surface.

From a numerical point of view, calculating turbulent flow past a bluff body and with active flow control (AFC) is quite a challenge, especially when oscillatory rather than steady state blowing actuation is used. First of all, since the slot is typically rather narrow, it is necessary to have strong grid refinement around the slot. Moreover, the high slot velocity might severely restrict the size of the timesteps for methods that treat the convective terms explicitly. Also, the rapid oscillation makes it more difficult for the pressure to converge in a Poisson pressure equation solver. The numerical results presented in this paper should be seen as preliminary. A more thorough investigation about bluff bodies (tilt-rotor aircraft airfoils) using the same numerical procedure has been carried out in Kjellgren[3].

2. Experimental Procedure

The investigation was carried out in a cascade wind tunnel with a test section that is 1.04 m wide 0.61 m high and 2.44 m long with a two dimensional nozzle and a contraction ratio of 7:1.

The vertically mounted cylinder (compare Figure 1) has a diameter of 76 mm with a 0.4 mm wide slot, inclined to the surface at approximately 30° to the downstream direction, which results in an almost tangential excitation. It is coupled on both ends to an external actuator consisting of two combined and modified loudspeakers, driven by a 2x660W amplifier.

The data was taken at 7 m/s, which gives a Reynolds number of 36,000. The natural shedding occurs at a Strouhal number of 0.2. This gives a natural shedding frequency of approximately 20Hz. The pressure distributions were measured by means of a multi-channel pressure scanner (Scanivalve ZOC23B). The PIV data was taken with a commercial system manufactured by Integrated Design Tools, using a Spectra Physics PIV200 NdYAG laser together with a digital Kodak ES 1.0 camera with a resolution of 1024x1024 pixels. A 60mm lens with a large aperture was used to get images with minimal distortion and sufficient contrast.

For seeding the flow a custom made particle generator was used together with the commercial "Standard Fog Fluid", made by ROSCO. For most experiments Δ_t=15µs was used for the delay between the two individual exposures which are necessary to get one set of PIV data. This allowed in the given situation to use window sizes down to 16x16 pixels for the cross correlation.

The level and quality of the excitation were tested on a bench-top calibration to verify its two-dimensionality and to determine the frequency and amplitude response of the actuator. The calibration was done by positioning a hotwire probe in the middle of the slot such that the blowing and suction peak were identical. This avoided problems usually caused by rectification. Therefore it was sufficient to take only the peak velocity to determine the level of the zero-mass-flow periodic excitation. Only single frequency sinusoidal input was used, so the obtained peak velocity was simply divided by √2 to get

the RMS value of the velocity in the slot. For the calculation of C_μ, a top-hat velocity profile was assumed. This leads to:

$$C_\mu = 2\, u_{RMS}^2\, b\, /\, U_\infty^2\, d$$

During the experiments the calibration procedure was refined to ensure a minimized scatter. This scatter (compare Figure 1 and 2 -- 110°, 150Hz at = C_μ 0.04) is caused by the fact that the level of excitation is very dependent on the temperature of the whole system. For this reason the internal pressure in the cylinder was taken as calibration reference.

The choice of an external actuator limited the useable frequency range from 50 to 250Hz, respectively F_r^+ (based on the radius) of 0.3 to 1.4, due to the frequency response of the excitation system. Frequency and C_μ sweeps were carried out over the full range for different slot positions. Different streamwise positions of the slot were used in this investigation in order to be able to obtain clearly distinguishable PIV results of the type shown in Figure 6.

The position of the excitation is most important for the general characteristics of active flow control. The maximum obtainable C_l/C_d depends on this parameter (see Figure 2) as well as the frequency needed to reattach the flow. The more downstream the slot is located the larger is the distance between the separated flow that develops into a free shear layer further downstream, and the convex surface. Therefore a higher C_μ is required to get the flow reattached, as was determined by Darabi[4] for a straight surface. For this reason an optimum frequency is needed for a given, limited C_μ.

A slot located at 100° allows full reattachment at low C_μ over a wide range of frequencies, whereas a location at 110° shows a strong dependence on frequency (Figure 2). In both cases, it is possible to get reattachment at the given relatively low C_μ in contrast to the setup with the slot placed at 120°, where no reattachment could be obtained at similar levels of excitation. The more downstream location of the excitation results in a slightly higher C_l/C_d, caused by the so larger attached region, provided that reattachment can be achieved. In every one of the cases investigated the reattachment was initiated at first upstream of the slot, enclosing a large separation bubble around 90° (Figure 3 -- C_μ=0.09, f=100Hz, θ_{slot}=120°) provided the C_μ was sufficient to force reattachment. At higher forcing levels this bubble shrinks and the flow reattaches downstream of the slot as well, but there may still remain a small separation bubble right downstream of the slot that disappears at sufficiently large C_μ.

The sensitivity of the flow to the frequency of excitation depends on C_μ and in particular on its lower values as shown in Figure 3. For a $C_\mu \geq 0.06$ no major differences in C_l/C_d for the chosen frequencies could be observed at the slot position shown. Below this value a better performance for higher frequencies (F_r^+ = 0.8 resp. 1.1) can be noticed. This might be due to the fact that the smaller structures upstream of the slot may amplify faster attaining the required threshold amplitude further upstream when the flow is forced. Once the flow is reattached upstream of the slot this region can be considered as saturated.

Therefore, no more major dependence on the frequency can be noticed after a certain threshold in C_μ has been reached.

In Figure 4 the corresponding pressure distributions are presented. The two distributions at 100Hz ($F^+_r=0.5$) clearly show the influence of the slot location. At 120° the flow separates although C_μ is increased from 0.06 to 0.09 creating a separation bubble upstream of the slot. This bubble can be avoided by adapting the forcing frequency to a more suitable value for this slot location and for the given C_μ. Although the pressure distribution on the slotted side changes significantly the changes on the opposite side are marginal. The base pressure however decreases from $C_p=-1.2$ to $C_p=-0.5$ even when the flow on the upper surface contains a large separation bubble ($C_\mu=0.09$, f=100Hz and $\theta_{slot}=120°$). The separation location on the opposite side did shift slightly upstream for the slot being located at 110°.

The velocity profiles presented in Figure 5 show a variation in time, depending on the phase of the excitation, downstream of the slot at 112° and at 90°. This cannot be observed at 75°, which is shortly after the location were separation occurs in the unforced case. On the surface that is opposite to the slot location (not shown here) no phase dependence was observed. The variation of u_{max} at 90° is approximately ±3% of the mean value whereas at 112° it is +4% and –7% of the mean. This relatively strong decrease in the velocity is caused during the suction phase of the excitation. It is remarkable that the blowing phase is only of this little influence, especially if one considers the small difference of only 0.03 to the phases of 0° and 270°.The boundary layer thickens between 75° and 90° about one third with about 10% higher u_{max} at 90° and 112°, meaning that the excitation compensates the loss of momentum through deceleration. The velocity profiles have been extracted from phase locked and ensemble averaged PIV data. Measurements could therefore only be carried out with forcing. Despite the good quality of the PIV data these profiles have to be seen more as showing tendencies because of the limitations of PIV in the near-surface region. These are caused by reflections on the surface of the body that can overpower the individual particle images and thus rendering the data at some locations near to the surface unreliable.

Some PIV results that were phase locked and ensemble averaged are shown in Figures 6a and 6b. In both cases the most interesting data out of a whole forcing cycle was chosen. Changes in the flow field with different excitation are clearly visible in the upper phase averaged images, indicating that there is a significant change on the bottom surface where the slot is positioned. There is hardly any change on the opposite side of the cylinder. With the higher level forcing, the vortices shed from the lower (forced) surface are more stable and coherent. The smaller coherence at lower levels of excitation is caused by vortex pairing at some distance from the cylinder. This can be observed clearly in the time series of the phase locked data. When excited at a higher level the flow separates further downstream, which results in a C_l/C_d approximately 2.5 times larger for $C_\mu=0.15$ compared to a C_μ of only 4%. Changes in the flow field on the side opposite of the slot can be observed from 0.5d downstream onwards.

The individual images shown in Figure 6 (bottom) give a good example for the high spatial resolution attained and the possibilities for further investigation of the vortex dynamics involved in the process of vortex shedding and flow reattachment. In Figure 6c the formation of two counter-rotating vortices during the suction phase is shown in an instantaneous vorticity field. The size of these vortices is in the order of magnitude of the coherent structures shown above. In contrast to the ensemble averaged data the rolling up of the vortex sheet of the separated boundary layer into a larger counter clockwise rotating vortex can be observed.

The instantaneous data presented in Figure 6d was taken a short time later in the excitation cycle. The clockwise rotating vortex has moved out of the shown field of view and had been supposedly weakened as can be deducted from the streamlines on the right border of the figure. The counterclockwise rotating vortex, formed out of the rolled-up vortex sheet of the separated boundary layer, has grown and stabilized.

3.   Computational Procedure

Both the unforced and the forced cases were calculated with an unstructured grid, semi-implicit, fractional step, finite element method. The method solves the Navier-Stokes equations, and uses Lilly's[5] modification for the dynamic coefficient Smagorinsky model. The coefficient was averaged in the homogenous direction which was sufficient for robust and reliable calculations. For derivation and details about the method, see Kjellgren[3].

The finite element method uses tri-linear weighting- and interpolation functions for the velocities, and a constant function is used for the pressure. An explicit four-steps Runge-Kutta scheme is used for the time stepping of the convection terms, while the diffusion terms are calculated by a slightly modified Crank-Nicholson method. The matrix equation arising from the implicit treatment of the diffusion terms is diagonally heavy and is solved with just a few iterations of a generalized Jacobi method. For the convection terms to be numerically stable, the Courant number is kept at ~2 throughout the calculations by an auto timestepper.

For the cases shown here, the size of the computational domain is typically 20 x 16 x 0.5 chords. The width in the spanwise direction, 0.5 chords, is not sufficient to be able to use periodic boundary conditions. Therefore, slip-walls are used as boundary conditions. The small width in the spanwise direction reduces the computational requirements, but likely causes the flow to have too little three-dimensionality. However, the main characteristics of the flow still seem to be adequately handled. It was chosen in that way so that a good spanwise resolution can be achieved with a relatively small number of nodes.

The slot was modeled by setting the oscillatory velocity as a Dirichlet boundary condition on the cylinder surface. Here, a top-hat velocity profile at a certain angle to the cylinder surface was used.

Figures 7a and 7b show pressure contours for the unforced case and forced cases, and Figure 7c shows the instantaneous velocity vectors. The calculations are carried out at a Reynolds number of 36,000, and the plots are from the middle of the span (z=0.25 diameters). About 400,000 nodes were used for the cases shown. Notice how the instantaneous velocity field in the case of Figure 7c remains attached to the surface even after having passed the slot. As for the cylinder wake, it is noticeably diverted similarly to the averaged PIV data in Figures 6a and 6b, and the vortices resulting from the forcing are seen in Figures 6a and 6b as well as in Figures 7b and 7c. Furthermore, the small vortices coming from the side of the cylinder opposite of the slot that are clearly seen in the calculations are seen as a "smeared" out shear layer in the phase locked and ensemble averaged PIV data.

4.   Conclusions

The pressure distribution and eddy structure of the flow around a circular cylinder can be altered significantly by means of periodic excitation through a slot located downstream of $90°$. The position of this slot determines the main characteristics of the excitation such as optimum forcing frequency and maximum C_l/C_d for a given forcing level.
The asymmetric application of active flow control leads to a large change in the pressure distribution on the side where the forcing is applied, whereas the influence on the opposite side is marginal with the exception of the change of the base pressure level. The direct influence of the periodicity of the excitation on the velocity profiles is limited to the region on the excited side where separation occurs naturally. The location of the excitation downstream of $90°$ assured that there was no forced transition in the shear layer, and therefore separation was controlled directly.

Active flow control gives the possibility of changing the drag and lift on a circular cylinder in a wide range, allowing the flexible adaptation of the flow to required properties in a wide range of technical applications. PIV is particularly suitable for investigation of the vortex dynamics leading to the reattachment of the flow. It also gives a very exciting opportunity to compare experimental data with computational results in the entire flow field. The descriptions of the vortex dynamics agree well between the computational and the PIV data.

References

[1] B. Nishri and I. Wygnanski.
Effects of Periodic Excitation on Turbulent Flow Separation from a Flap.
AIAA Journal 36:547-556, 1998.

[2] A. Naim, A. Seiffert and I. Wygnanski.
Active Control of a Cylinder Flow with and without a Splitter Plate using Piezoelectric Actuators.
AIAA Paper 2002-3070, 2002.

[3] P. Kjellgren, D. Cerchie, L. Cullen, and I. Wygnanski., Active Flow Control On Bluff
Bodies With Distinct Separation Locations.
AIAA Paper 2002-3069, 2002.

[4] A. Darabi.
On the Mechanisms of forced Flow Reattachment.
PhD Thesis, University of Tel Aviv, 2001

[5] D.K. Lilly.
A Proposed Modification of the Germano Subgrid-Scale Closure Method.
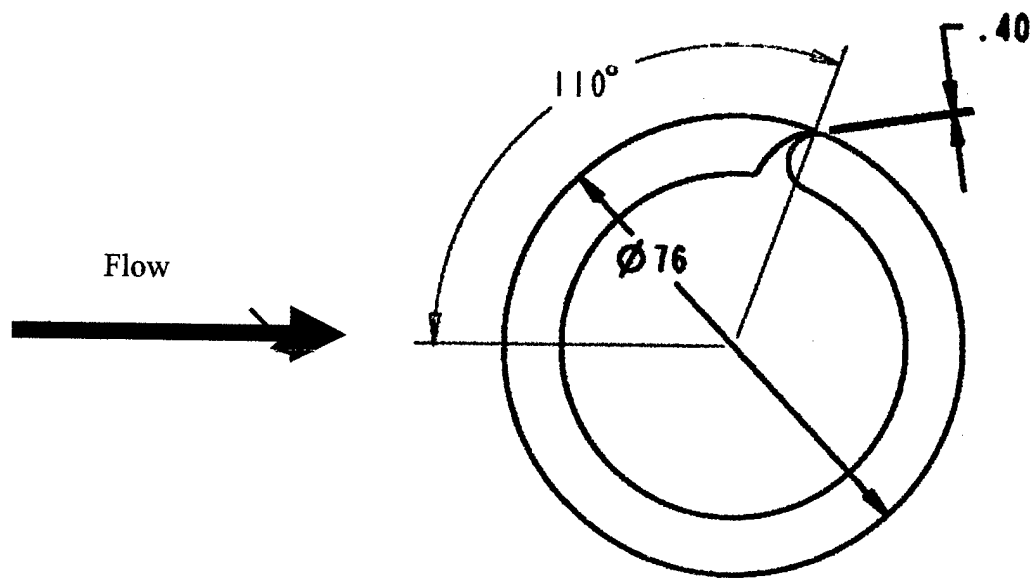*Phys. Fluids A 4(3), 633-635, 1992.*

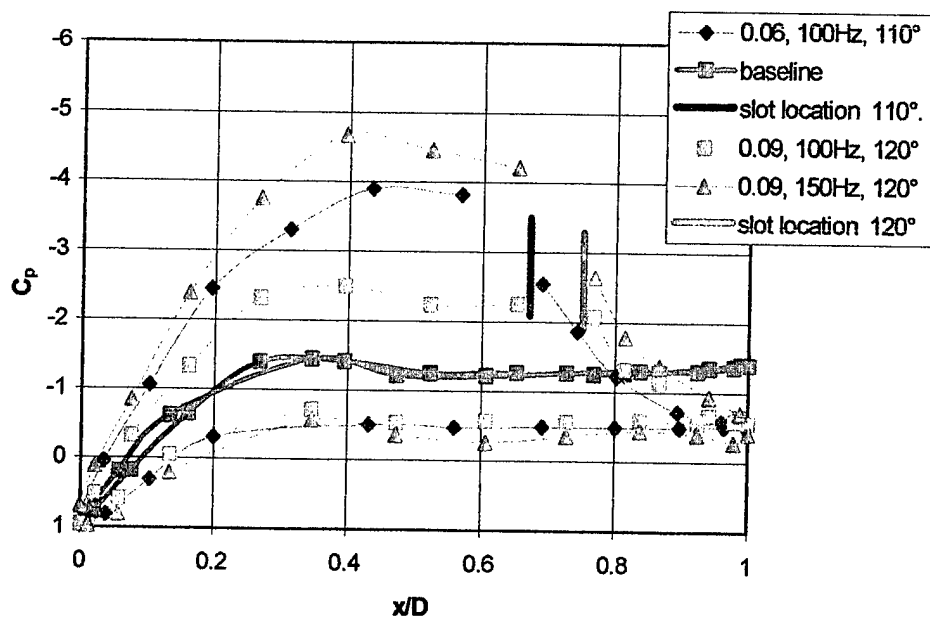**Figure 1 Cylinder with slot and positions of pressure taps**
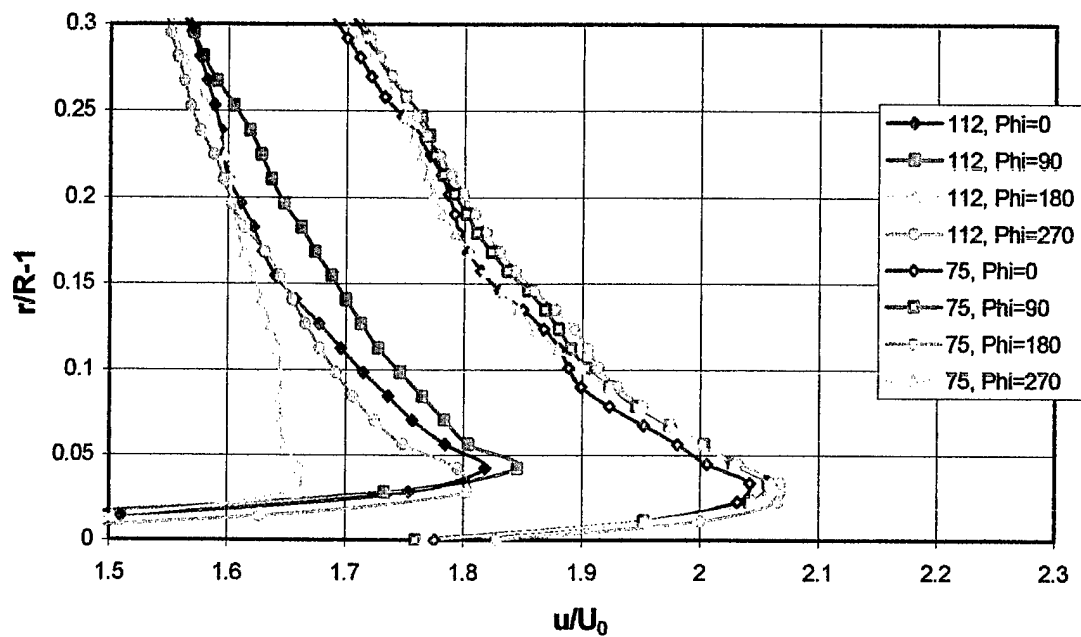

Figure 4: Forcing at varying C_μ , Slot at 110° and 120°

Figure 5a: Velocity profiles at 75° and 112°, Slot at 110°, C_μ=0.07
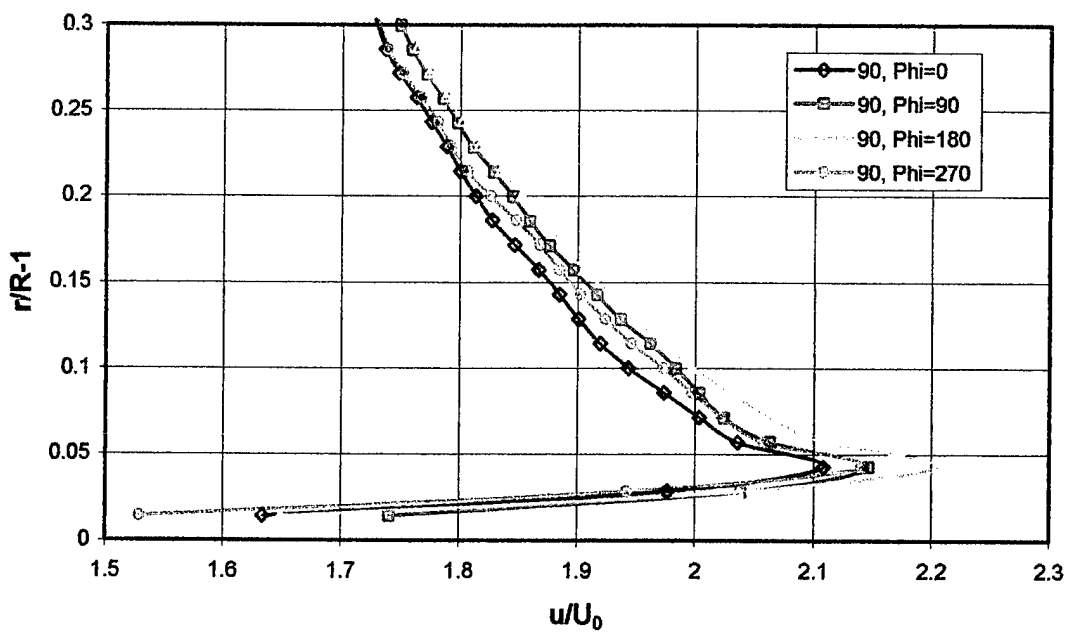
Figure 5b: Velocity profiles at 90°, Slot at 110°, C_μ=0.07
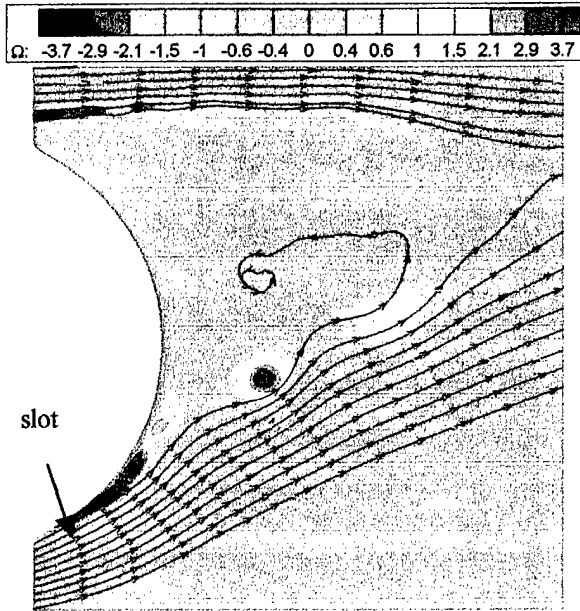
Figure 6a: Slot at 110°, F^+_r=0.8, C_μ=0.15
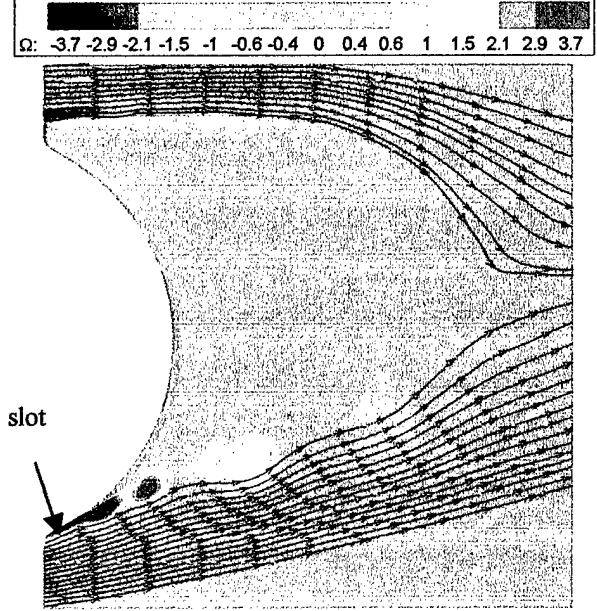
Figure 6b: Slot at 110°, F^+_r=1.1, C_μ=0.04
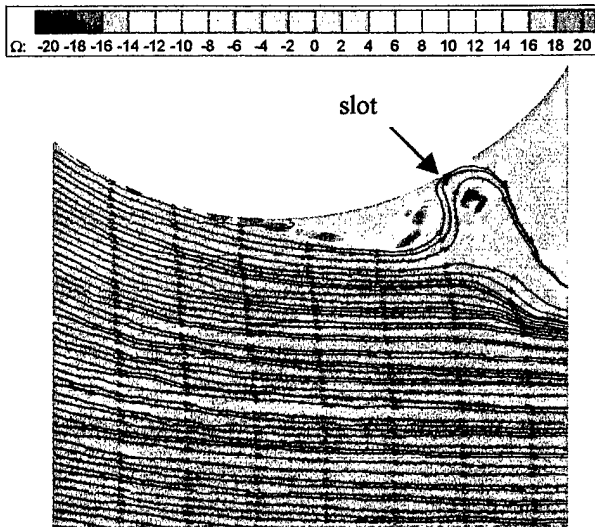
Figure 6c:Instantaneous data, suction phase
Slot at 120°, F^+_r=0.7, C_μ=0.07
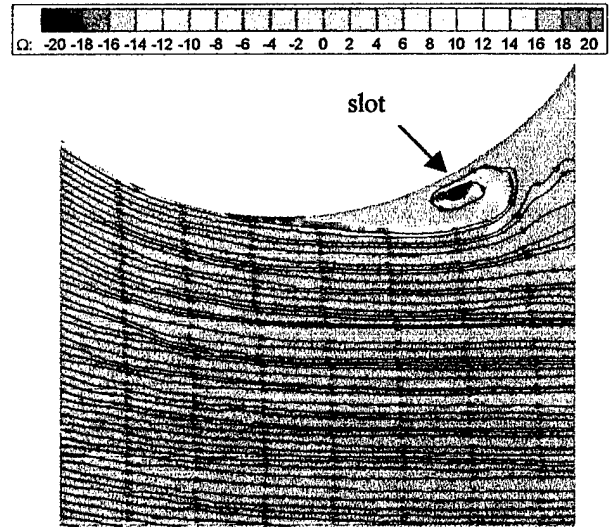
Figure 6d: Instantaneous data
Slot at 120°, F^+_r=0.7, C_μ=0.07
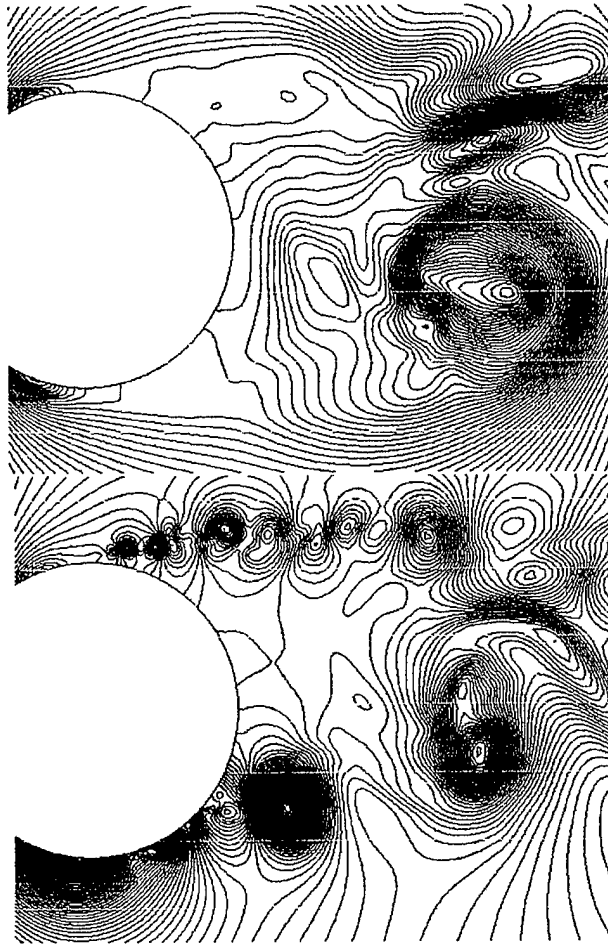
Figure 7 Computed pressure contours for a cylinder at Re=36,000. a) Without AFC b) With AFC c) Velocity vectors for the forced case (below)

Forcing slot

With AFC
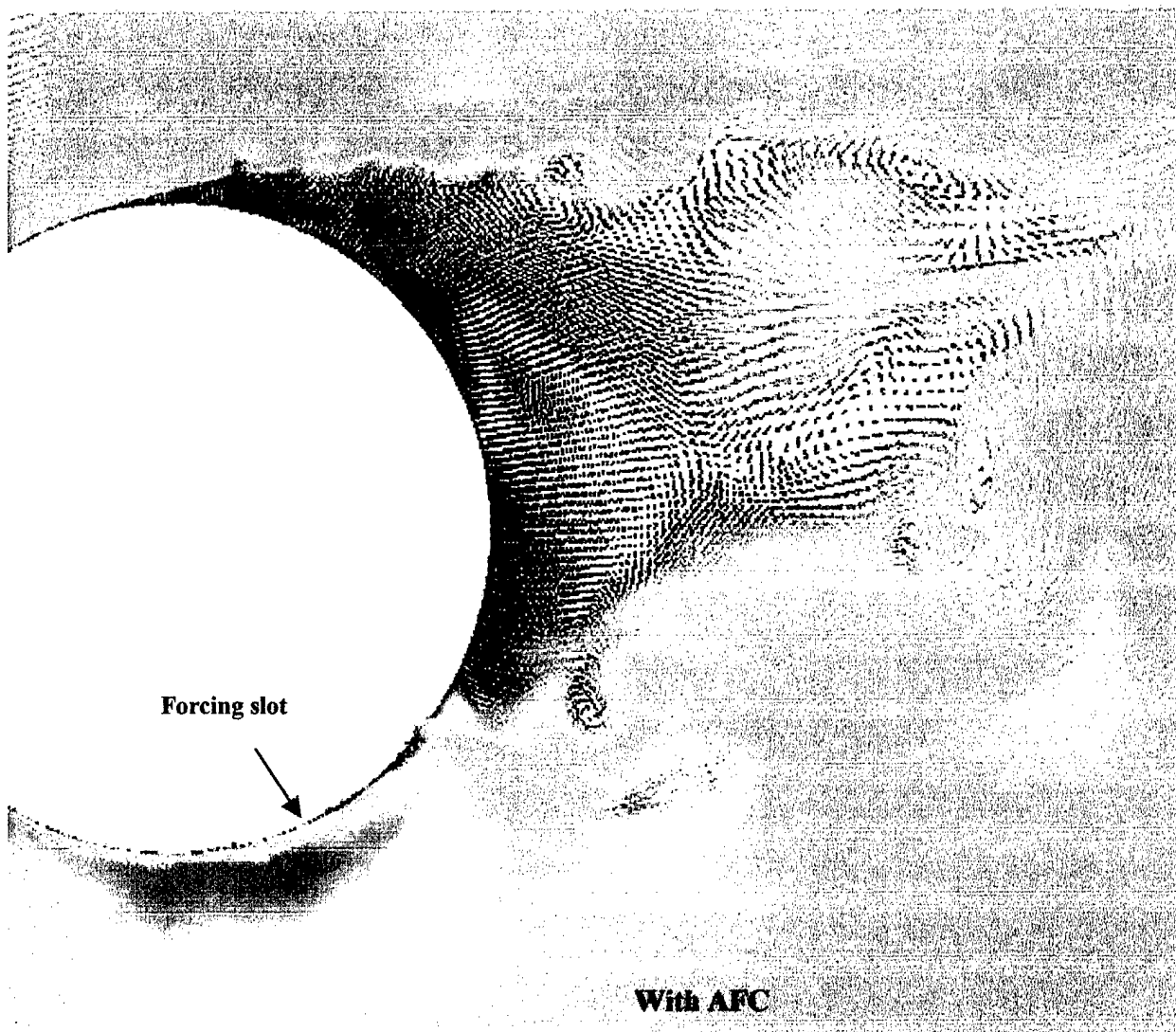
ACTIVE FLOW CONTROL ON A DIVERGENT-TRAILING-EDGE AIRFOIL

The underlying idea of this research was to assess the ability of local AFC (i.e. where the actuation is located at the trailing edge) to control the wake generated downstream of a bluff trailing edge of a lifting airfoil and thus improve its performance. Furthermore, to assess the long range effects of AFC generated near the leading edge on this configuration, and finally to investigate the interaction between these two sources of actuation. In this report only some integral aerodynamic characteristics are discussed while detail particle image velocimeter (PIV) investigation is being prepared.

A NACA 0012 airfoils was modified to have a divergent trailing edge (DTE) as shown in Figure 1. The basic airfoil was chosen because of the availability of its aerodynamic performance at the low Reynolds numbers of interest. The trailing edge thickness is 2.5% of the chord and it represents an equivalent to a typical Gurny flap. A fillet, tangential to the lower surface some 8% of the chord upstream deflects the local flow by an angle of 15° to the chord at the trailing edge.
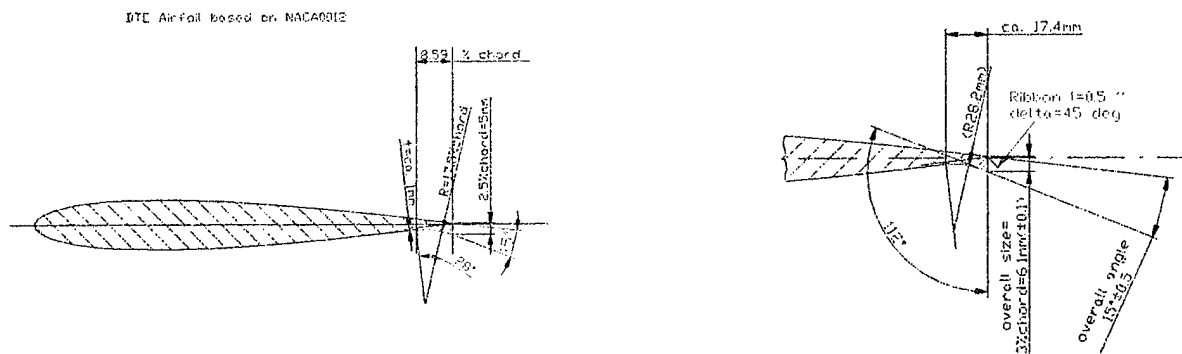

Figure 1: The DTE Airfoil

The aerodynamic characteristics of this airfoil are given in below and they are compared with the conventional NACA-0012 airfoil. Most of the experiments were carried out at a low Reynolds number (Re≈90,000). The addition of the DTE moves the C_L-α to the left providing a C_L=0.45 at α=0° and increasing the maximum C_L attained from 0.95 to 1.2. The stall characteristics of the airfoil became much gentler due to the DTE modification. Although the drag penalty at low values of C_L is substantial (about 20% at C_L=0.5), the addition of the DTE enables one to loiter at C_L=1.

A tiny fliperon was added to the airfoil at the trailing edge that was hinged to it at the upper surface. The fliperon does not exceed the 2.5% chord so it can be stowed when not in use. It is mainly intended to reduce drag at moderate values of α by interacting with
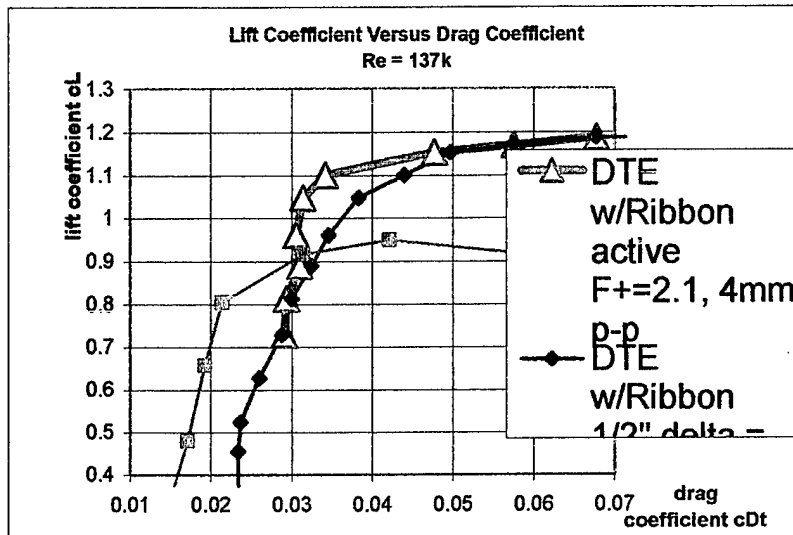

Figure 2. A drag-polar for the DTE airfoil with and without active fliperon and comparison with NACA0012

the "near wake" coherent structures. In fact when the fliperon (ribbon) was activated the total drag was reduced for $C_L>0.8$. The maximum (L/D) ratio attained was 35 and was comparable to the best performance of the clean NACA 0012 airfoil at the same Re but it occurred at a $C_L>1.05$ instead of at $C_L>0.75$. This is advantageous and it can be used either to lower the loiter speed or to increase the useful carrying load.

A slot milled near the leading edge of the airfoil provided traditional active flow control by a massless jet (this is sometimes referred to as a synthetic jet). It was intended to be active mostly at high angles of attack in order to delay stall. A comparison of pressure distributions at $\alpha=12^0$ indicates that the flow is separated over the entire upper surface at $C_\mu<1\%$, at a higher momentum coefficient partial attachment was achieved that turned into a total attachment when $C_\mu>3\%$. It is known, that a fairly sharp leading edge airfoil requires a much higher C_μ to force the flow to reattach than an airfoil with a more rounded leading edge (e.g. NACA0015). The precise significance of the leading edge radius of curvature in this case remains to be assessed.
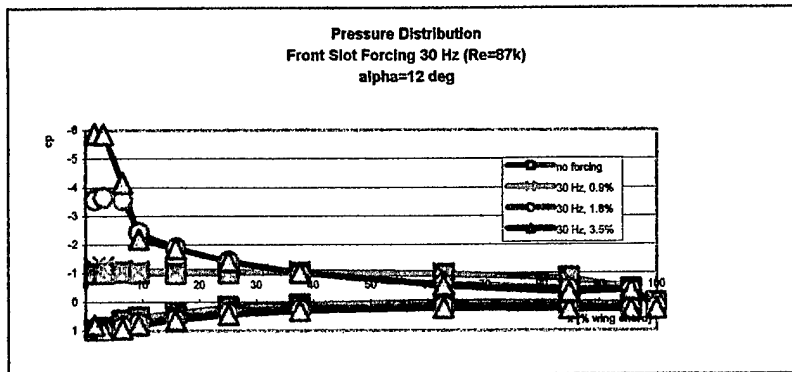
Figure 3. The pressure distribution over a DTE airfoil.

The Aerodynamic characteristics of this DTE airfoil with and without the use of AFC are shown in Fig 4. The maximum lift coefficient had increased from 1.2 to 1.6 & 1.7 depending on the frequency of the actuation. The drag of the basic airfoil that hovered around $C_D=0.024$ for $C_L<1$ turned into thrust $C_T=0.011$ at $C_L=0.9$. This implies that entire jet momentum was recovered as thrust. In this case then, the application of AFC resulted in a lift increase that exceeded 40% while the $C_\mu = - C_D$.

The combined excitation from the leading and trailing edges turned out to be detrimental as far as the thrust recovery is concerned suggesting that the phase relation between the two actuators have to be carefully controlled. The optimum frequency ratio between the two actuators appears to be 2:1.
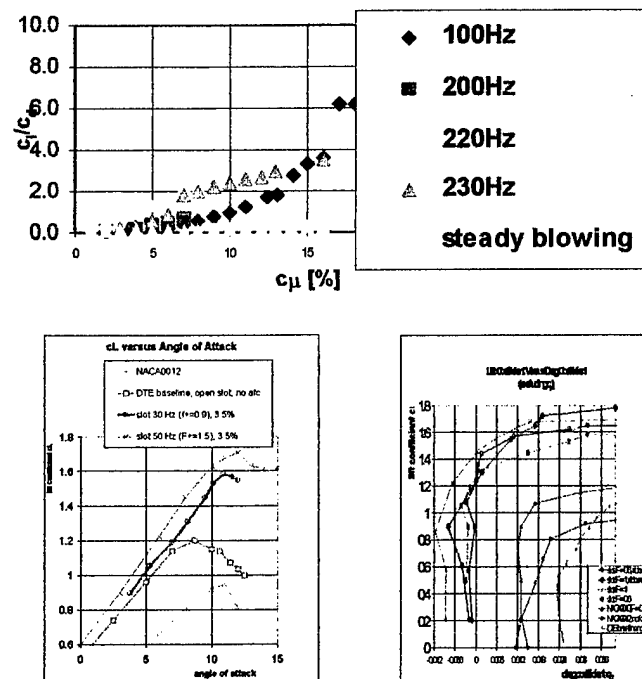

Figure 4. The improvement in the aerodynamic performance of a DTE airfoil due to AFC applied at the leading edge.

45

Personnel Supported

Olaf Lisser	Graduate Student, University of Arizona, Tucson
Lutz Taubert	Graduate Student, Technical University of Berlin
Per Kjelgren	Research Associate, University of Arizona, Tucson
I. Wygnanski	Professor, University of Arizona, Tucson

Publications

1 G. Han, A. Tumin, and I.Wygnanski, "Laminar Turbulent Transition in Poiseuille Pipe Flow Subjected to Periodic Perturbations Emanating from the Wall" Part 2. Late Stage Transition *J. Fluid Mechanics* **419**, 1-27, 2000

2 K. Elsberry, J. Loeffler, M.D. Zhou & I. Wygnanski, "An Experimental Study of a Boundary Layer that is Maintained on the Verge of Separation" *J. Fluid Mechanics* **423**, 227-262, 2000

3 Ming de Zhou and I.Wygnanski, " The response of a mixing Layer Between Parallel Streams to a Concomitant Excitation at Two Frequencies" *J. Fluid Mechanics, August, 2001*

4 Neuendorf, R. Likhachev, O. and Wygnanski, I.,On " Streamwise Vortices in a Convexly Curved Turbulent Wall Jet" *Accepted for publication in Physics of Fluids, 2000*

5 Greenblatt, D. and Wygnanski, I, "Control of separation by periodic excitation", *Progress in Aerospace Sciences*, Volume 37, Issue 7, pp. 487-545, 2000.

6 Greenblatt, D., Neuburger, D., Wygnanski, I., "Dynamic Stall Control by Intermittent Periodic Excitation", *AIAA Journal of Aircraft, Vol. 38, No. 1, 2001 (to appear).*

7 Greenblatt, D. and Wygnanski, I., "Use of Periodic Excitation to Enhance Airfoil Performance at Low Reynolds Numbers" *AIAA Journal of Aircraft, Vol. 38, No. 2, 2001 (to appear).*

8   Greenblatt, D., Nishri, B., Darabi, A. and Wygnanski, I. "Dynamic stall control by oscillatory addition of momentum. Part I: Mechanism" *AIAA Journal of Aircraft, Vol. 38, No. 3, 2001* .

9   Greenblatt, D. and Wygnanski, I. "Dynamic stall control by oscillatory addition of momentum. Part II: Parametric Study", *AIAA Journal of Aircraft, Vol. 38, No. 3, 2001*

CONFERENCE PROCEEDINGS & CHAPTERS IN BOOKS

1. Y.Guy, J.A. Morrow, T.E.McLauglin and I.Wygnanski., "Velocity measurements on a delta wing with periodic blowing and suction," AIAA Paper 2000-0550, 38th Aerospace Sciences Meeting Reno NV, 2000.
2. H. Fasel, A. Ortega, & I.Wygnanski , "Film Cooling in a Pulsating Stream-Recent Results for Laminar and Turbulent Wall Jet," 18 Symposium on Energy Engineering Sciences ; Argonne National Laboratory May 2000
3. P. Kjellgren, N. Anderberg and I. Wygnanski, "Download Alleviation by Periodic Excitation on a Typical Tilt –Rotor Configuration-Computation and Experiment," AIAA Paper 2000-2697.
4. I. Wygnanski, "Some New Observations Affecting the Control of Separation by Periodic Excitation," (Invited paper), AIAA Paper 2000-2314
5. A. Darabi, L. Lourenco & I. Wygnanski, " On the Mechanism of Flow Reattachment by Periodic Excitations" in Advances in Turbulence VIII,
   p. 201-204 C.Dopazo (ed.) CIMNE, Barcelona. (Proceedings of ETC 8, Barcelona June 2000)
6. M. Hites, H. Nagib, T. Bachar and I.Wygnanski " Enhanced Performance of Airfoils at Moderate Mach Numbers Using Zero-Mass Flux Pulsed Blowing," AIAA 2001-0734, Jan. 2001.
7. E. Gutmark, B.Callender, B.A.Anderson, T.R.S. Bhat and I Wygnanski, "Jet Noise Suppression Using Flexible Filaments," (invited) AIAA 2001-0371 Jan. 2001.

Awards Received
The AIAA Fluid Dynamics Prize "..for pioneering work and leadership in active flow control"
Transitions
Active control of separation is undergoing transition research to the V-22 "Osprey",Quad Rotor Project, the XV-15 airplane, helicopter rotors and UAV technology.